Modeling of Soot Formation in Turbulent Diffusion Flames Impinging on a Cold Surface

Roytor Charoensin-O-larn

A dissertation
Submitted in partial fulfillment of the
Requirements for the degree of

Doctor of Philosophy

University of Washington
2022

Reading Committee:
John C. Kramlich, Chair
Jonathan D. Posner
Alberto Aliseda

Program Authorized to Offer Degree:
Mechanical Engineering

University of Washington

Abstract

Modeling of Soot Formation in Turbulent Diffusion Flames Impinging on a Cold Surface

Roytor Charoensin-O-larn

Chairs of the Supervisory Committee:

Professor John C. Kramlich
Department of Mechanical Engineering

Soot is well known to be hazardous to both health and the environment. Over 40% of the world's population relies on biomass-fueled stoves for cooking, and these stoves are a significant source of soot. Especially problematic is the direct exposure to soot experienced by the user during cooking. The biomass-fired cookstove application often involves the impingement of a diffusion flame on the relatively cold cookware surface. Earlier experimental work showed that soot emissions increased substantially during flame impingement. This study seeks an improved understanding of the mechanisms responsible for this observation. The work primarily uses modeling as the tool to identify the mechanism. The approach focuses on two areas. The first is the development of an improved model for the oxidation of soot by O_2 that includes a more realistic temperature dependence than has heretofore been presented in the literature. This is hoped to address the problem of

overprediction of soot oxidation that appears in many modeling results. The second part consists of a broader study of reactive soot dynamics during the impingement process.

Detailed soot models reflect the four processes governing soot dynamics: nucleation, surface growth, coagulation, and oxidation. Several studies have reported that the modeling of soot oxidation by O_2 is inaccurate as it tends to overpredict the oxidation rate resulting in an underprediction of emissions. One of the challenges with modeling the oxidation process is that as the particle ages in the flame, it becomes more crystalline in structure and becomes less reactive to oxidation. The parameter α is widely used to represent this aging process wherein the soot surface reactivity ranges from $\alpha = 0$ (nonreactive) to $\alpha = 1$ (fully reactive). The surface deactivation process has been modeled primarily by using in-flame soot measurements for developing functional forms and parameters to describe the decay of surface reactivity, α. Among these, the model developed by Appel et al. has been widely used. Several studies indicate that the aging process should depend on both temperature and exposure time. Nevertheless, the time-temperature history of the particle is not directly taken into account in the model of Appel et al. A more recent model proposed by Khosousi et al. introduces a new parameter called the thermal age which incorporates the temperature-time history of the particle into the aging process. The model is, however, empirically based and does not reflect the non-linear temperature dependence one would expect of the physics of such a process. The present work presents a new soot aging model that is based on the framework of the well-studied problem of coal char oxidation deactivation. With a more fundamental framework, including the more realistic Arrhenius temperature dependence for the deactivation rate, the present model provides a better basis for approaching a wider range of flames. The new model is configured to provide the same parameter α so that it can be easily applied to existing soot models. The new approach is implemented in the fixed-pivot sectional soot model, with the model showing improved agreement with literature flame data.

As mentioned above, soot emissions were found to increase substantially in cookstove experiments when the flame impinged on the cooking pot. Pundle et al. studied this phenomenon by examining emissions when an ethylene/air turbulent diffusion flame impinged on a cold pot surface compared to the system without the pot. The ethylene flame was used because it is a sooting flame with an extensive free flame database. (This particular study was the first in the literature to examine the problem of soot emissions resulting from flame impingement.)

The present study computationally examines this configuration to identify the mechanisms leading to emission enhancement. The study uses a computational fluid dynamics code, a detailed chemical kinetic mechanism that includes soot precursor species, the laminar flamelet model to provide the turbulence/chemistry coupling problem, and the sectional model to simulate the soot dynamics. To reflect the experimental setup, the computational flame impinges on a surface at 373 K. The presence of the surface potentially affects soot behavior via (1) heat extraction by the surface leading to quenching of the chemical reactions, and (2) distortion of the flow field/mixing rates caused by the presence of the surface. To test this, runs were made in which the surface was assumed to be adiabatic, thus eliminating the heat extraction component. Very broadly, the insertion of the adiabatic surface leads to (1) an enhancement of local soot concentrations upstream of the surface, and (2) a decrease in soot concentrations as the flow diverges around the surface. In both cases, this results primarily from the alteration of the flow field. The initial increase in soot concentrations results from the surface causing an enhancement of the local turbulent scalar dissipation rate. The increased mixing rate leads to enhanced C_2H_2 concentrations which increase soot concentrations by promoting the surface growth process. The later decrease in soot concentrations occurs when the surface forces the flame to spread around itself forming a thinner concentration boundary layer which allows more O_2 to diffuse in. This process enhances the O_2 oxidation process at the location of the surface causing a sharp decrease in the in-flame integrated soot flux. The net result, however, is an enhanced emission.

One concern in the cookstove literature is that adopting emission control strategies may lead to a reduced particle size for the remaining emissions, this potentially increasing the health impacts. This was experimentally examined by Pundle et al. who obtained size distribution measurements as part of the surface impingement work. The particle number density grows in all size ranges as the surface moves away from the fuel nozzle. This behavior occurs when the surface is located near the fuel nozzle ($\leq$ 245 mm). However, there is no difference in the shape of the size distribution nor in the peak diameter. As the surface moves further away, the 245-mm case has fewer small-sized particles than the 300-mm case. The coagulation process is found to be responsible for the observed behavior as the 300-mm case has more space for particles to disperse resulting in lower concentration and lower coagulation process.

Acknowledgment

This thesis would not have been possible without the support of marvelous individuals. I would like to express my sincere gratitude to my advisor, Professor John C. Kramlich for his continuous support, invaluable advice, and patience during my PhD study. His abundant experience and immense knowledge have encouraged me throughout my academic research. My gratitude extends to Professor Jonathan D. Posner for his support and wise suggestions. I would like to thank Professor Alberto Aliseda for serving on my committee and for his numerous inputs. I wish to thank Professor James C. Hermanson for serving on my committee. Furthermore, I would like to thank Professor James J. Riley for his continual support of my fluid mechanics knowledge throughout my PhD course. I would also like to thank Professor Philip C. Malte for his valuable inputs as well as his provision of the computational resource.

I would like to thank Anamol Pundle for his mentorship, guidance, and support. I also wish to thank Wanwisa Kisalang for her support during my PhD life. I also would like to thank other people whom I did not mention here, I appreciate their support and contributions to this work.

I would like to thank my parents and my girlfriend for motivating me to take on this PhD track and giving me strength throughout my study.

Table of Contents

List of Figures

List of Tables

Chapter 1

Introduction

1.1 Overview and Motivation

The mechanisms of soot formation and behavior in flames have been an active research topic for many years. This arises due to (1) the well-recognized impact on health associated with the inhalation of soot emissions [1], (2) the importance of soot to the radiative heat balance within flames, and (3) the important role soot plays in atmospheric heat balances. The diffusion or non-premixed flame configuration is the only flame that generally produces soot in practical systems. Although many engineering applications utilize premixed flames to reduce emissions, there are circumstances where the diffusion flame configuration is unavoidable, of which cookstoves are an important example. According to the World Health Organization, 42% of the world's population relies on biomass stove cooking [11] which contributes to a significant amount of soot production. Soot behavior in a non-premixed flame is sensitive to the fuel and the way the combustion process takes place. A good understanding of fundamental soot behavior in the diffusion flame is essential to the development of strategies for reducing emissions. Due to the complex behavior of soot in such flames, modeling is widely used to help understand and interpret the mechanisms of soot production and destruction.

One of the challenging aspects of soot modeling is capturing the loss of the reactivity of the soot towards oxidation as the soot ages in the flame. Thus, this thesis starts with developing a more fundamental soot deactivation model which is expected to be more robust and can be applied to a broader range of flames than the available models.

Inserting a cold surface into a hydrocarbon diffusion flame results in soot deposits on the surface. This is the basis for the carbon black industry. More recently work on biomass cookstoves has shown that when the flame impinges on the bottom of the pot, the emission of soot in the combustion gas increases substantially. Note that this is different than simply the collection of soot deposits on the pot surface. This impingement occurs through either overfiring the flame resulting in a long flame length, or placing the pot too close to a correctly-fired flame [5]. The behavior of soot emissions occurring when a non-premixed flame impinges on a cold surface has not yet been investigated or reported in the literature. Therefore, this thesis aims to understand the mechanisms behind these experimental results. The work attempts to separate the parallel effects of heat transfer (i.e., thermal quench at the surface) and fluid dynamics (i.e., enhanced flame strain near the surface).

This thesis is organized as follows. Chapter 1 discusses the importance of soot emission control in diffusion flames which motivates the need for accurate modeling of soot behavior.

A literature review of soot modeling and the relevant chemical mechanisms is included in this chapter. Chapter 2 provides the development of a more realistic model for the reduction in O_2 surface oxidation rates via soot surface aging. The model is validated by comparison against experimental data from the literature for in-flame soot behavior. This newly developed model is then used to conduct the study for the next chapter. Chapter 3 presents the study of soot behavior occurring when the flame impinges on a cold surface. In this chapter, the simulation results are provided along with experimental data [5]. Furthermore, the investigation result is detailed to show the mechanism which is responsible for the variation in soot behavior when the flame impinges on a surface. The study is continued in Chapter 4. The chapter investigates the mechanism responsible for the in-flame soot behavior which is observed in Chapter 3 as well as the influence of inserting a cold surface into the flames on the particle size distribution function. The effect of heat transfer and surface location are examined. Chapter 5 covers the conclusion of the present work as well as suggesting the study worth investigated in the future.

1.2 Literature Review

This section consists of 2 subsections. The first subsection provides a literature review for general soot behavior, while the second subsection centers on a review of soot modeling.

1.2.1 Review of soot formation

There are numerous soot formation pathways proposed based on various soot precursor molecules, including polyacetylene [12] and polycyclic aromatic hydrocarbons (PAH) [13]. The consensus among most of the researchers in the field is that polycyclic aromatic hydrocarbons are the precursors of the soot particle [14]. In the combustion process, small aliphatic molecules are generated before they develop into aromatic rings. Several pathways have been suggested for such a process, with more detail provided in [14]. Among these, recent experimental studies show support for the even-carbon-atom pathways. PAHs are also suggested to be generated through a multi-ring formation process, thus, the growth rate of PAHs is not limited by single-aromatic-ring formation [14].

The "H-abstraction-C_2H_2-addition" mechanism (HACA), proposed by Frenklach et al. [15] is generally accepted as the main growth mechanism of PAHs toward soot formation. This HACA mechanism contains 2 steps. The first step is to remove a hydrogen atom from a PAH molecule forming a radical site on the PAH molecule,

$$A_i + H \rightleftharpoons A_{i-} + H_2 \tag{1.1}$$

The second step is to add an acetylene molecule to the radical PAH,

$$A_{i-} + C_2H_2 \rightarrow products \tag{1.2}$$

Even though the H-abstraction step can be achieved by several means, experimental evidence suggests that such a process is dominated by H-atoms [14]. Besides acetylene, other growth species have been proposed including methyl, propargyl, and cyclopentadienyl [16]–[18]. Nevertheless, simulation by Frenklach et al. argues that all different growth pathways relax to the acetylene addition process [19]. With this repetitive HACA process, PAHs continue to grow toward a large size and eventually become a soot particle.

As PAHs grow, they eventually cross a somewhat arbitrary boundary that divides a large molecule from a small particle. This particle generation step is called nucleation. Thus, nucleation marks the point where PAHs change from the gas phase to a solid soot particle. This process was first assumed to occur due to pure chemical growth by acetylene [20].

This proposal yields accurate soot masses, yet, the particle size is significantly underpredicted. Many recent studies define nucleation to occur due to the collision between PAHs rather than via molecular growth. Frenklach et al. proposed that the dimerization of pyrene molecules causes particle inception [14] which is widely adopted by many studies.

The surface of nascent soot particles then reacts with gas species to increase particle size. This process is called surface growth. Acetylene has been found via experimental studies to be the main growth species for such a process and it is believed to follow first-order kinetics [14]. This process occurs at the particle surface which is assumed to be analogous to the edge of large PAHs. Therefore, the particle surface is covered by C-H bonds which makes the HACA mechanism capable of describing the process. Following the PAH mechanism, the soot particle growth process starts by abstracting an H atom from the particle surface leaving a surface radical site. The radical site then reacts with acetylene forming a larger particle [14]. Such a process can be expressed as follows,

$$C_{soot-H} + H \rightleftharpoons C_{soot\cdot} + H_2 \qquad (1.3)$$

$$C_{soot\cdot} + C_2H_2 \rightarrow C_{soot-H} + H \qquad (1.4)$$

where $C_{soot\text{-}H}$ is the hydrogenated surface site and $C_{soot}\cdot$ represents the dehydrogenated site. Several studies note that the surface reaction rate decreases over time [1], [14], [21]. This is referred to as the surface aging process, which occurs due to a decrease in a number of active surface sites. More detail on the surface aging process can be found in Chapter 2.

While surface growth adds more mass to the particle, oxidation is a mass removal process that results in particle size reduction. O_2 and OH are found to be the main soot oxidizing species [14]. These act in a way that is similar to the surface growth process. It starts with H atom abstraction to activate the surface site followed by the reaction between the site and one of the oxidative species that removes a carbon atom from the particle surface. The oxidation reactions are illustrated by Equations (1.5) and (1.6),

$$C_{soot\cdot} + O_2 \rightarrow 2CO + products \tag{1.5}$$

$$C_{soot\cdot} + OH \rightarrow CO + products \tag{1.6}$$

The most commonly used kinetic rate for soot O_2 oxidation was derived by Nagle et al. [22]. The OH oxidation rate is normally adopted from the work of Neoh et al. [23].

Another important soot evolution process is coagulation. This process takes place due to the collision between two particles resulting in one larger particle. Initially, the coagulated particle adopts a spherical shape due to the high radii of curvature resulting in high surface energy and surface mobility. At later stages the surface mobility decreases, and the coagulation process results in particles with a more fractal-like shape [14]. Coagulation is a mass-conserving process; however, it changes the number of particles. The Smoluchowski equation from aerosol dynamics is generally used to describe this process [14].

1.2.2 Review of soot modeling

Given the complexity of the processes described in the preceding section, modeling is necessary to understand how the mechanisms adapt to the various environments provided by flames. Soot behavior simulations consist of two major components. These are (1) gas-phase chemical kinetics and (2) soot particle dynamics [24]. This is usually modeled in a one-way coupling format in which the homogeneous chemical kinetics influence the soot formation mechanisms, but the soot chemistry does not influence the gas-phase species. Several chemical mechanisms have been proposed to capture soot precursor species which include the detailed chemical kinetic model, *The FORCE*, which contains 192 species and 1896 reactions, including the PAH formation pathways that are relevant to soot formation [25]. The most common modeling format for the gas phase chemistry is the flamelet model, as this is a widely accepted means of modeling the fluid/chemistry interaction in turbulent diffusion flames. With this approach, reasonable calculation times can be achieved for the gas chemistry and fluid dynamics. The resulting values for the temperature and species concentrations are then used as inputs to the soot particle dynamics calculation. This approach is widely reported in the literature [20], [26], [27]. The soot dynamics is then specifically solved with this information.

The soot particle dynamics can be obtained by solving the particle population balance equation (PBE) [28]. There are several approaches that can be used to solve the PBE, which include the method of moments [29], and the sectional method [24], [28], [30]. The method of moments was first introduced by Frenklach et al. in which certain particle size distribution moments are solved instead of solving for the distribution itself [29]. This method trades computational speed and memory in place of the ability to directly calculate the detailed soot size distribution. There are 2 types of moments developed in their study. The first one is the concentration moment which defined as,

$$M_r^{soot} = \sum_{i=1}^{\infty} m_i^r N_i^{soot} \tag{1.7}$$

where M_r^{soot} is the r^{th} concentration moment of the particle size distribution, i is the size class of the particle, m_i represents the particle mass of the particular size class, and N_i^{soot} is the particle number density [29]. The number of carbon atoms was used as a means of representing soot particle mass. By solving differential equations for concentration moments, desired information of the particle size distribution can be acquired, e.g., the zeroth moment represents the total particle number. Another class of moments are called size moments,

$$\mu_r^{soot} = \frac{M_r^{soot}}{M_0^{soot}} \quad (1.8)$$

This type of moment is useful for calculating derived quantities, for instance, the first size moment is the average particle size. Such an approach significantly reduces computation time [29]. However, only statistical information, e.g., total particle number, mean, and variance of the particle size distribution, can be obtained [26].

The sectional method solves the particle population balance equation by discretizing the size distribution into finite "bins". The interactions between the bins simulate the evolution of the size distribution. This approach yields particle size distribution information, but it requires substantially more computational resources [26]. In order to reduce the computational time required for the sectional method, the fixed-pivot sectional method was developed [31]. The fixed pivot technique is achieved by dividing the soot particle size distribution into a fixed number of sections [30] with one size representing the whole section [31]. Another approach to this problem is the moving-sectional technique. In this method, the representative sizes change to follow the surface growth rate. By doing this, numerical diffusion from the surface growth process can be avoided. This technique, however, requires that new sections to be continuously created for the nascent particle from nucleation. Thus, the rearrangement of sections is vital to keep the number of sections feasible for the calculation [28]. The present study uses a fixed-pivot sectional method; hence, the following literature review focuses on this technique.

As mentioned in the previous section, the evolution of soot behavior is the result of nucleation, coagulation, surface growth, and oxidation processes [14]. The nucleation process is normally modeled by either the dimerization of pyrenes [14] or the purely chemical growth with acetylene acting as a nucleating species [20]. Among these, the mechanism that identifies the nucleation event as the collision of 2 pyrenes has been adopted by several recent studies due to its ability to predict the particle size more accurately [14]. The source term of nucleation by pyrene dimerization can be expressed by this equation,

$$\dot{\omega}_{nuc} = 2.2 \times \sqrt{\frac{4\pi k_B T}{m_{pyrene}}} \times D_{pyrene}^2 \times N_{av}^2 \times [C_{16}H_{10}]^2 \qquad (1.9)$$

where $\dot{\omega}_{nuc}$ represents the particle nucleation rate which provides mass into the smallest size section, *2.2* is the van der Waals enhancement factor, k_B is Boltzmann constant, T is the temperature, m_{pyrene} is the molecular mass of pyrene molecule, D_{pyrene} is the effective diameter of each pyrene molecule, and A_v is Avogadro's number [30].

Surface growth is based on the widely used H-abstraction-C_2H_2-addition mechanism (HACA) [1], [14]. This process is modeled by the two-point method which can be written,

$$\dot{\omega}_{i,sg} = \frac{R_{sg,i-1}N_{i-1}}{v_i - v_{i-1}} - \frac{R_{sg,i}N_i}{v_{i+1} - v_i} \qquad (1.10)$$

which $\dot{\omega}_{i,sg}$ is the surface growth source term, $R_{sg,i}$ is the particle growth rate, N_i is particle number density, and v_i is the particle size which can be mass or volume, for the i^{th} size section [28]. Equation 1.10 is responsible for moving particles from one bin to the next. The particle surface growth rate, $R_{sg,i}$, can be calculated by the following equations,

$$R_{sg,i} = \alpha k_4 [C_2H_2][C_{soot^\circ}] \qquad (1.11)$$

Where α represents the fraction of surface sites available for reaction [3], [29], k_4 is the reaction rate constant which can be calculated from Table 1.1 shown below, $[C_{soot^\circ}]$ represents the concentration of dehydrogenated surface sites [3] which can be calculated from,

$$[C_{soot^\circ}] = \frac{A_s}{N_{av}} \chi_{Csoot^\circ} \qquad (1.12)$$

where A_s is the total surface area of the particle and N_{av} is the Avogadro's number [3], $\chi_{Csoot^{\circ}}$ is the number of radical sites per unit surface area which can be calculated by assuming a steady state for $C_{soot^{\circ}}$ from the reactions in Table 1.1,

$$\chi_{Csoot^{\circ}} = \frac{(k_1[H]+k_2[OH])\chi_{Csoot-H}}{k_{-1}[H_2]+k_{-2}[H_2O]+k_4[C_2H_2]+k_5[O_2]} \tag{1.13}$$

where $\chi_{Csoot-H}$ is the number of site C_{soot-H} density which is estimated to be 2.3×10^{15} site/cm^2 [3], [29].

Table 1.1

HACA-based soot surface growth and oxidation reactions [1], $k = AT^n e^{-E/RT}$

No.	Reaction	A (cm^3 mol^{-1} s^{-1})	n	E (kcal/mol)
1	$C_{soot}\text{-}H + H \leftrightarrows C_{soot}^{\cdot} + H_2$	4.2×10^{13}		13.0
2	$C_{soot}\text{-}H + OH \leftrightarrows C_{soot}^{\cdot} + H_2O$	1.0×10^{10}	0.734	1.43
3	$C_{soot}^{\cdot} + H \rightarrow C_{soot}\text{-}H$	$2.0 \text{ x } 10^{13}$		
4	$C_{soot}^{\cdot} + C_2H_2 \rightarrow C_{soot}\text{-}H + H$	$8.0 \text{ x } 10^{7}$	1.56	3.8
5	$C_{soot}^{\cdot} + O_2 \rightarrow 2CO$ + products	$2.2 \text{ x } 10^{12}$		7.5
6	$C_{soot}\text{-}H + OH \rightarrow CO$ + products	$\Gamma = 0.13$		

Soot surface oxidation is modeled similarly to the surface growth process as they are both based on the reaction between the particle surface and gaseous species. By adopting the two-point method, the soot oxidation process can be modeled as follow,

$$\dot{\omega}_{i,ox} = \frac{R_{ox,i}N_i}{v_i - v_{i-1}} - \frac{R_{ox,i+1}N_{i+1}}{v_{i+1} - v_i} \tag{1.14}$$

where $\dot{\omega}_{i,ox}$ represents the particle oxidation source term, $R_{ox,i}$ is the particle oxidation rate which is always negative, for the i^{th} size section [28]. As mentioned, there are 2 main oxidizing species which are O_2 and OH. The oxidation rate of both reactions are modeled differently as particle oxidation by O_2 is based on Nagle Strickland-Constable's work [22] while the oxidation process by OH is widely modeled to follow the study of Neoh et al. [23].

Similar to the surface growth process, the oxidation rate by O_2, $R_{ox,O2}$, can be expressed by the following equations,

$$R_{ox,O2} = \alpha k_5 [O_2][C_{soot^\circ}] \tag{1.15}$$

where k_5 is the reaction rate constant which can be calculated from Table 1.1 while α represents the ratio of the available surface site for the reaction. The oxidation process by OH, however, is generally modeled based on the collision probability between the particle surface area and OH molecule [23], [32],

$$R_{ox,OH} = \gamma \sqrt{\frac{8RT}{\pi m_{OH}}} A_s [OH] \tag{1.16}$$

where γ is defined to be 0.13 based on Neoh et al.'s work [23], and A_s is particle surface area.

While surface reactions determine the soot mass in the system, the coagulation process influences the number of particles. The coagulation process is normally modeled to follow the well-known Smoluchowski equation [14], [26]. Such a process is generally modeled in the sectional method as,

$$\dot{\omega}_{i,coag} = \frac{1}{2} \sum_{j+k=i} \beta_{jk} N_j N_k - N_i \sum_{k=1}^{\infty} \beta_{ik} N_k \tag{1.17}$$

where the first term on the right represents the birth term of the particle in i^{th} size section by the coagulation between particles from the j^{th} and k^{th} size section. The second term on the right determines the number of particles leaving the i^{th} size section as they coagulate with another particle. For the free-molecular regime, β_{jk} is the coagulation kernel which can be calculated from [33],

$$\beta_{jk} = \left(\frac{3}{4\pi}\right)^{\frac{1}{6}} \left(\frac{6k_B T}{\rho_{soot}}\right)^{\frac{1}{2}} \left(\frac{1}{v_j} + \frac{1}{v_k}\right)^{\frac{1}{2}} \left(v_j^{\frac{1}{3}} + v_k^{\frac{1}{3}}\right)^2 \tag{1.18}$$

where v_j is the volume of the j^{th} size section, and ρ_{soot} is the particle density which is widely defined to be 1800 kg/m^3 [34]. Since each size section is represented by one fixed size for the fixed-pivot sectional method, there is a possibility that the coagulation process results in the formation of a new particle whose size falls between two pivots. Kumar et al. developed an approach to resolve this issue such that both particle number and mass are conserved [31]. This can be achieved by assigning fractions a and b to satisfy these equations,

$$a(v_i)f_1(v_i) + b(v_{i+1})f_1(v_{i+1}) = f_1(v) \tag{1.19}$$

$$a(v_i)f_2(v_i) + b(v_{i+1})f_2(v_{i+1}) = f_2(v) \tag{1.20}$$

where f_1 and f_2 represent the number and volume of particles respectively, and v is the volume of a new particle resulting from the coagulation process which $v_i \leq v \leq v_{i+1}$ [31].

1.3 Statement of Objectives

Even though significant work has gone into the development of the understanding of soot behavior in flames, there are gaps in the understanding that have not been reported in the literature. The work reported in this dissertation addresses three issues regarding soot behavior in flames: (1) an alternative model for the age-related deactivation of soot towards O_2 oxidation, (2) the mechanisms responsible for the enhancement of soot emissions when a flame impinges on a cold surface (motivated by cookstove studies), and (3) the influence soot reduction strategies on the size distribution of the soot that is produced.

While most of the active processes in soot dynamics appear to be accurately modeled, several studies indicate that improvement is still required for the oxidation process. Specifically, as the soot particles age within the flame, they become less reactive towards O_2 oxidation. Current models of this process tend to be empirical and thus do not generalize well across a broad range of flames. In Chapter 2 we describe the development of a more fundamentally based surface deactivation model.

In Chapter 3, the influence of placing a cold surface into the turbulent diffusion flame is computationally examined by using the surface deactivation model developed in Chapter 2. One goal is to understand the behavior that is experimentally observed when flames impinge on the cooking pot surface during cookstove experiments. The process is influenced by both heat transfer to the surface and by the modification of the fluid dynamics caused by the straining of the flame at the surface. The present work attempts to deconvolute the contributions of these processes.

Chapter 4 extends the work from Chapter 3 to investigate in-flame integrated soot flux behavior via the evaluation of the contributions of the various mechanisms responsible. This chapter also computationally studies the effect of the impinging flame on a the particle size distributions produced by the flame.

Chapter 2

Soot Thermodeactivation Model Development

2.1 Overview

This chapter presents the development of a new element for the models used to predict soot behavior in ethylene flames. The objective of this work is to develop a fundamental surface aging/deactivation model for O_2 oxidation which is expected to be more robust and can be applied to a wider range of flames than the currently available empirical models. The development is motivated by the observation that the rate of the soot oxidation by O_2 is normally overpredicted by the current models. This results in underpredicted in-flame soot volume fractions and underprediced emissions. This chapter starts with a literature review of the soot oxidation process by O_2, and the particle surface aging process. The available models for predicting the aging effect are introduced followed by the development of a new model in this work. The developed model is validated against literature data for in-flame soot volume fraction prediction. The performance of a developed model in emission prediction is also verified with experimental data which the results can be found in Chapter 3.

2.2 Literature Review

Soot oxidation by O_2 is one of the processes most in need of improvement as it is generally overpredicted by the available models [2]. As mentioned in Chapter 1, the process is typically modeled as a surface reaction between O_2 and an active surface site with an Arrhenius temperature dependence for the reaction rate,

$$R_{ox,O2} = \alpha k_5 [O_2][C_{soot^\circ}] \tag{2.1}$$

The fraction of surface sites available for the reaction is known to decrease as the particle ages [1], [2], [21], [35]. This fraction of active sites relative to total sites is the parameter α. The literature reports several models for the decrease in α that account for the influence of both time and temperature. These are discussed in Section 2.3.

Soot particle aging is a complex process that has been investigated by several research groups. Among these, Vander Wal et al. experimentally studied the influence of soot particle nanostructure on soot oxidation by O_2 [36]. In this study, extensive differences in soot nanostructure were observed as the soot was heat treated at various values of temperature and time. They proposed that the soot particle consists of a stack of graphene layers which agrees with recent observations from Frenklach et al. [37]. These graphene layers are initially stacked in random directions with respect to each other as the particle structure is amorphous [36]. Reactions can take place both at the basal plane and the edge of the graphene layer. The reactivities are known to be significantly lower at the basal plane than at the edge site.

This is supported by the work of Smith et al. which found that the graphitized carbon requires a higher temperature for the oxidation to occur at a significantly slower rate compared to that of non-graphitized carbon [38]. Similar to other carbon-rich materials, the accessible sites for the H-abstraction process are potentially at the free reactive carbon edge. For the nascent soot particle, the number of free-edge sites is expected to be high as graphene layers are randomly arranged. After exposure to the high-temperature environment, the free-edge sites rearrange and start to bond with adjacent graphene layers resulting in less reactive edge sites [36]. This process is generally referred to as the graphitization or "aging" which describes the rearranging in the particle structure toward a more crystalline graphite-like structure.

Apart from the soot particle, other carbon-rich materials also exhibit this surface aging process. One system that has received significant attention is coal char. The char surface deactivation problem has been studied extensively due to its importance for char burnout in boilers [10], [39], [40]. The decay rate of char surface reactivity toward O_2 oxidation has been modeled using the time-temperature history of the particle. The process is termed thermodeactivation or thermal annealing [10]. Several approaches have been proposed to cover this thermodeactivation of carbon surfaces, including defining an aging coordinate whose rate follows an Arrhenius-type relation [39]. Senneca et al. studied the effect of heat treatment on the reactivity of carbon surfaces with O_2 and CO_2 [10]. The carbon samples were heat-treated at fixed temperatures in the range of 500 - 2000°C for different treating times and the reactivity was measured using an isothermal thermogravimetry technique [10]. In the same study, the thermodeactivation kinetic model from Salatino's work [39] was employed to fit the experimental data. In the model, the annealing coordinate ξ is defined such that ξ is 0 for the non-annealed char and becomes 1 for the fully annealed char. The reactivity is then defined as,

$$R = R_0(1 - \xi) + R_\infty \xi \tag{2.2}$$

where R is the instantaneous reactivity which is defined as the time required to achieve 50% char burnoff which has units of 1/s, R_0 is the non-annealed char reactivity and R_∞ is the fully annealed char reactivity which is assumed to be 0. The annealing coordinate ξ is assumed to change at a rate which follows an Arrhenius temperature dependence:

$$\frac{d\xi}{dt} = A_d \exp\left(-E_d/R_u T\right)(1 - \xi)^n \tag{2.3}$$

where A_d is a pre-exponential factor, E_d is the deactivation energy, R_u is the universal gas constant and T is the temperature. Equations (2.2) and (2.3) can be combined for n>>1, which yields the equation,

$$-\ln\left[\left(\frac{R}{R_0}\right)^{n-1} t\right] = \ln[(n-1)A_d] - E_d/RT \tag{2.4}$$

The study fitted the experimental data to the model to obtain values of each parameter [10], resulting in $n = 6.5$, $A_d = 4\times10^{21}$ s^{-1} and $E_d = 142$ kcal/mol. The similarity between 1-ξ and α should be apparent.

2.3 Present Models

As mentioned in the previous section, a number of approaches for modeling the α parameter have been proposed in an effort to provide a good agreement between simulation results and experimental data. The simplest model adopts constant values of α for each flame [29], [41], [42]. Using a constant value for α yields good results for soot behavior in a single flame. However, the value of α differs between flames, therefore, there is no single constant α exists that can accurately predict soot behavior in a variety of flames. This fact is supported by the computational study by Khosousi et al. [2]. Experimental observations suggest that α should be expressed as a function of residence time and temperature [2]. Kazakov and coworkers suggested a functional form of α which depends on the maximum temperature of the flame [35]. This model of α is an improvement from the constant value α. Nevertheless, such a functional form of α neglects the effect of particle residence time. Apart from the mentioned proposal for α, several more sophisticated models have been suggested. Among these, the model proposed by Appel et al. [1] and Khosousi et al. [2] are the most widely used in recent studies.

2.3.1 The ABF Model

As mentioned in Section 2.2, soot particle surface aging is suggested to be a both temperature-, and residence time-dependence process. Appel, Bockhorn, and Frenklach (ABF) proposed a model of α which is a function of local temperature and particle size [1]. The study was conducted based on the several laminar premixed flames which are listed in Table 2.1.

Table 2.1

Summary of Flame Conditions

Flame Designation	Pressure (bar)	Fuel	Composition (mol %) Fuel	O_2	N_2 or Ar	Gas Velocity (cm/s)	[C]/[O]	T_{max} (K)
WBF.12.3	0.12	C_2H_2	22.6*	12.4	55.0 Ar	20.1	1.30	1980
JW1.69	1	C_2H_4	12.66	18.34	69.0 N_2	5.9	0.69	1711
XSF1.78	1	C_2H_4	14.0	18.0	68.0 N_2	4.0	0.78	2104
XSF1.88	1	C_2H_4	15.5	17.4	67.1 N_2	6.5	0.88	1957
XSF1.98	1	C_2H_4	17.0	17.4	65.6 N_2	5.4	0.98	1908
JW10.60	10	C_2H_4	11.2	18.65	70.15 N_2	6.0	0.60	2017
JW10.673	10	C_2H_4	12.38	18.40	69.22 N_2	3.0	0.673	1895
JW10.68	10	C_2H_4	12.5	18.40	69.10 N_2	6.0	0.68	1880

* 10% of water vapor was added to the fuel stream.

It is important to note that this model was developed to track the reactivity of soot particles towards surface growth, which depends on the number of active sites available for reaction. The assumption is made that the same active sites host the O_2 oxidation reaction. Thus the model is widely used to track deactivation towards oxidation.

In sooting premixed flames, the main surface reaction is the surface growth process while the oxidation by O_2 is insignificant due to the very low O_2 concentrations in the flame. Therefore, the α developed in this study is based only on the surface growth process. In this study, the functional form of α was proposed as followed,

$$\alpha = \tanh\left(\frac{a}{log\mu_1} + b\right) \tag{2.5}$$

where a and b are parameters from the curve fitting process against the experimental data while μ_1 is the first size moment (average size) of the particle distribution which is defined in [29].

Instead of tracing for the residence time of the particle, the average particle size is used to represent the residence time. This is due to the assumption that the size of the particle is controlled by the surface growth process which is valid in premixed flames as more residence time implies more accumulated mass (i.e., a bigger particle size). The authors adjusted parameters *a* and *b* against the experimental soot volume fraction from 8 non-premixed flames.

Using this procedure, the best-fitted values of *a* and *b* were obtained for each flame with the results shown in Figure 2.1.

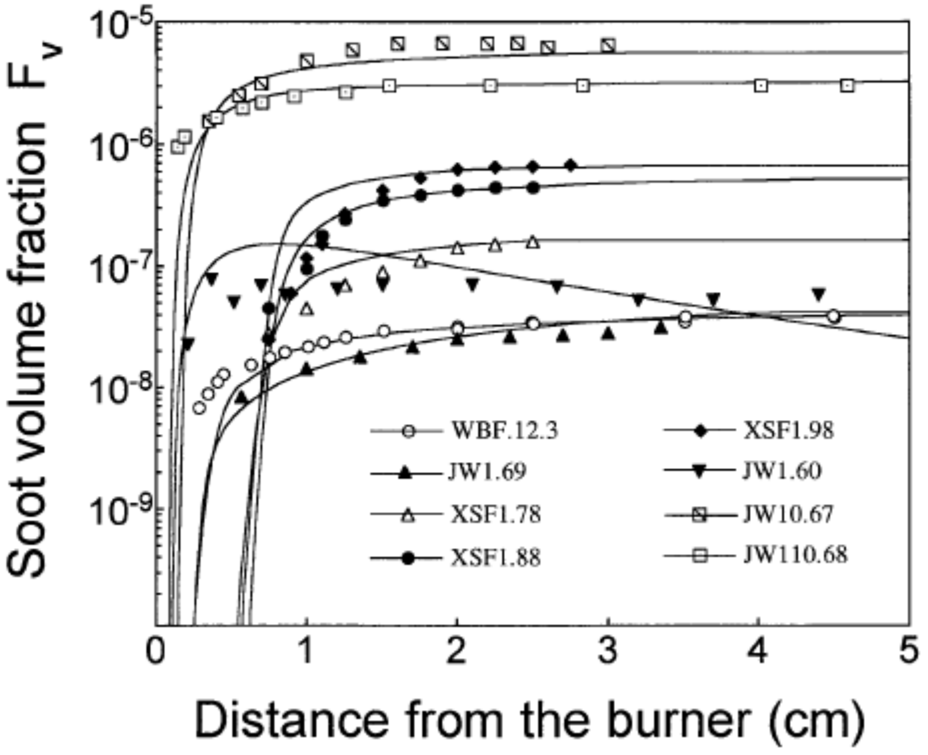

Figure 2.1. Soot volume fraction predicted (lines) with Equation (2.5) and experimental data (symbol) for the eight sooting laminar premixed flames [1].

Despite the good agreement between the predictions by model and experimental data, the modeling results shown in Figure 1 are limited in the sense that different values of *a* and *b* are derived for each flame. This limits the generality of the approach. Aiming to develop a generic functional form of α for all flames, Appel et al. found that parameters *a* and *b* have a straightforward correlation with the maximum flame temperature. Figure 2.2 presents the correlation between maximum flame temperatures and parameters *a* and *b*. The correlation shown in Figure. 2.2 provides a more general means of identifying *a* and *b* as correlated with the maximum flame temperature.

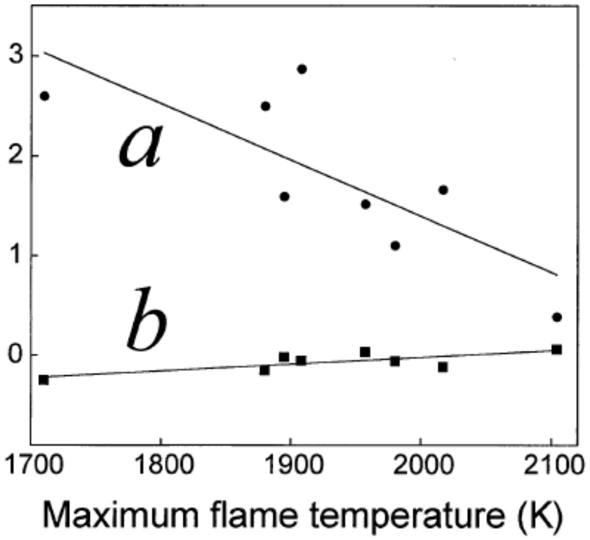

Figure 2.2. Correlation between parameters *a* and *b* of Equation (2.5) and the maximum flame temperature [1].

Under the assumption that the parameters *a* and *b* are linear functions of local flame temperature, the authors refitted the Equation (2.5) by optimizing soot volume fractions in all flames at once. The unified fitted solution can then be expressed,

$$a = 12.65 - 0.00563T \tag{2.6}$$

$$b = -13.8 + 0.00068T \tag{2.7}$$

where T represents the local temperature with the unit of K. The results of a new generic α model is shown in Figure 2.3.

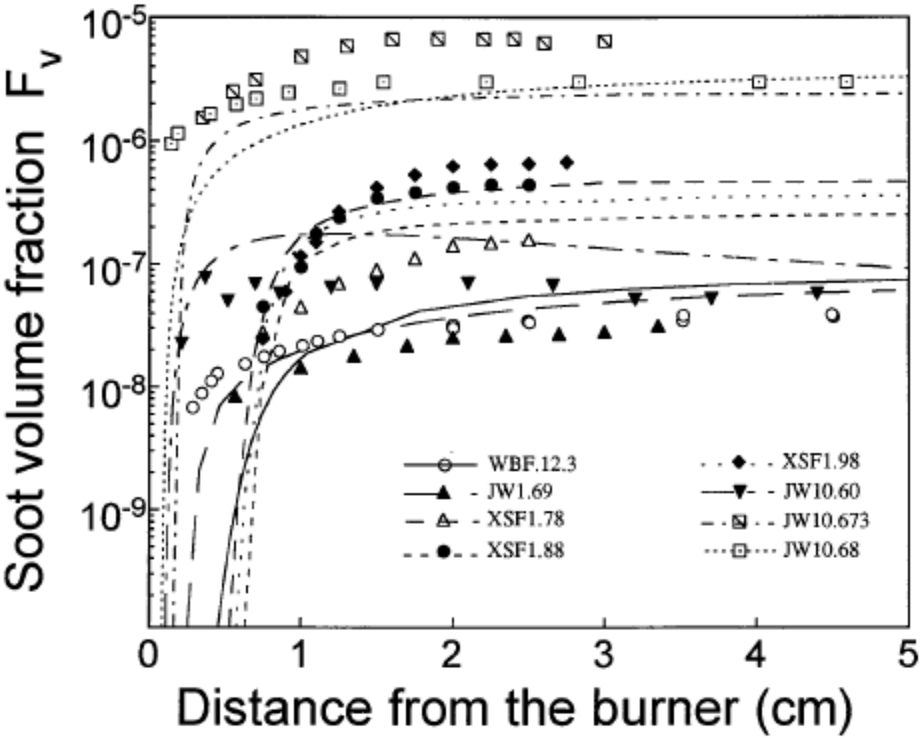

Figure 2.3. Soot volume fraction predicted (lines) with a general functional form of α and experimental data (symbol) for the eight sooting laminar premixed flames [1].

By comparing Figure 2.3 to Figure 2.1, it can be clearly seen that the deviation between simulation results and experimental data is increasing for the more general model. However, it is argued in the study that the maximum difference from this newly developed model is still within the factor of 3 [1], and that the correlation represented by Figure 2.3 now depends only on the single flame-dependent parameter of maximum flame temperature.

Due to the absence of other alternatives for an α model for soot oxidation by O_2, the model developed by Apple et al. [1] is widely adopted for soot oxidation, even though it was derived for surface growth. The rationale is that both processes operate on the same active sites that are represented by α. Nevertheless, several studies indicate that using the ABF model overpredicts the soot O_2 oxidation, which can eventually result in a significant underprediction in soot volume fraction [43]. Hence, there have been many efforts to develop new α models which predict the oxidation more accurately. One important candidate is the Thermal Age model from Khosousi et al. [2] which is discussed in the next section.

2.3.2 The Thermal Age Model

As discussed in the previous section, one of the recent proposals to model the aging process of soot particle is the Thermal Age model which was first presented in the work of Khosousi et al. [2]. In this study, the authors conducted a sensitivity analysis by altering the soot oxidation rate by O_2 and OH to isolate the effects of O_2 and OH oxidation. This produced the results shown in Figure 2.4.

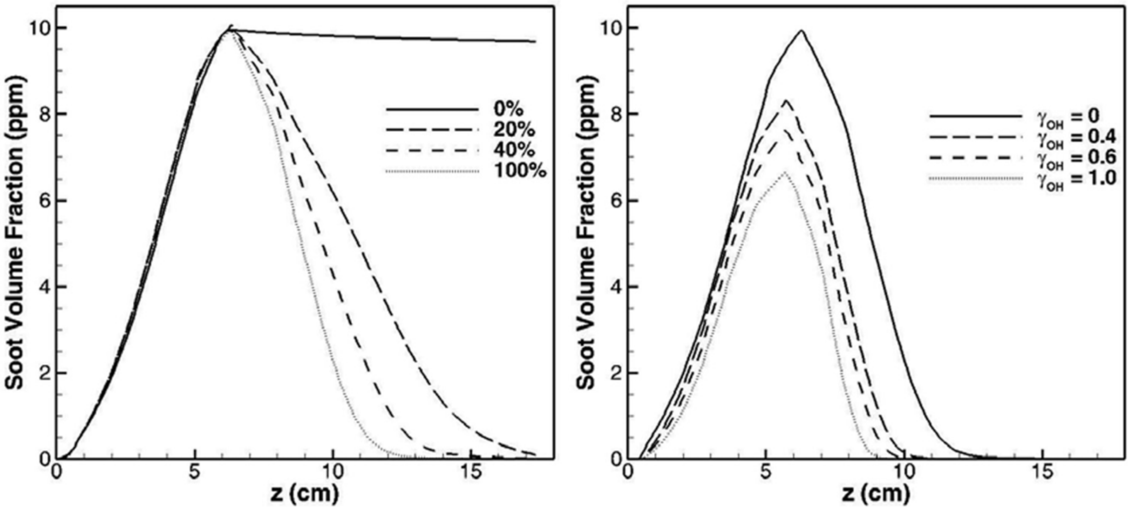

Figure 2.4. Soot volume fraction plots along the streak line exhibit maximum soot for variation of O_2 (left) and collision efficiency of OH (right) [2].

From Figure 2.4, the left panel shows that increasing the oxidation rate by O_2 notably reduces the amount of soot in the post-flame region but has a tiny effect in the soot formation region. On the other hand, it can be seen from the right plot that increasing the OH radical collision efficiency lowers the peak of the soot volume fraction. This is clear evidence supporting that oxidation by OH is significantly important in the in-flame region where soot particles are formed, and OH is present. The O_2 is, on the other hand, absent in the flame region. This approach allows the effect of oxidation by these two species to be studied separately. Since the OH oxidation rate proposed by Neoh and coworkers is widely used and accepted, the work of Khosousi et al. focused on soot oxidation by O_2. Due to the fact that oxidation by O_2 plays a major role later in the flame, the sensitivity of soot oxidation by O_2 can be studied by focusing on the post-flame region.

As mentioned in Section 2.2, soot particle surface aging is suggested to be both a time- and a temperature-dependent process [1]–[3], [15]. This was modeled by introducing a thermal age parameter, T_a [2], [3],

$$T_a = \int T dt \tag{2.8}$$

where T is the temperature, and t is the residence time over which the particle is exposed. To obtain T_a, each particle is tracked over its time-temperature history. The equation of α was obtained by correlating the relationship between α and T_a observed in flame data [2] using the procedure developed in the work of Veshkini et al. [3]. This was done by first obtaining the optimized constant value of α for each of the eight laminar non-premixed flames. The values of α were then plotted against a particle thermal age at the maximum area of soot concentration. An example from the work of Veshkini et al. [3] is shown in the left panel of Figure 2.5.

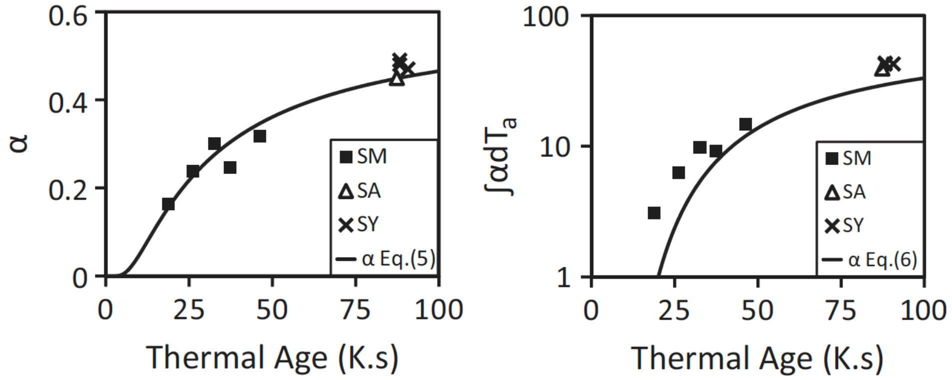

Figure 2.5. The plot of α, as a function of the thermal age of a particle at the maximum soot concentration (left). The plot of the integral of α against the particle thermal age at the maximum soot concentration (right) [3].

By curve fitting, the correlation between the parameter α and thermal age can be obtained. However, the α developed was only an average value of a flame and was not localized. Therefore, the optimized values of α were integrated along the pathline which exhibits the maximum soot volume fraction. The result is shown in the right panel of Figure 2.5. The curve fitting process was then performed yielding the relationship between $\int \alpha dT_a$ and T_a followed by differentiating such an equation with T_a [3]. The equation was then normalized by the thermal age at the point of maximum soot volume fraction in the flame, $T_{a,max}$, giving the final form of the equation,

$$\alpha = (\frac{T_{a,max}}{T_a})^2 \exp\left[2\left(1 - \frac{T_{a,max}}{T_a}\right)\right] \qquad (2.9)$$

Equation (2.9) is plotted as shown in Figure 2.6.

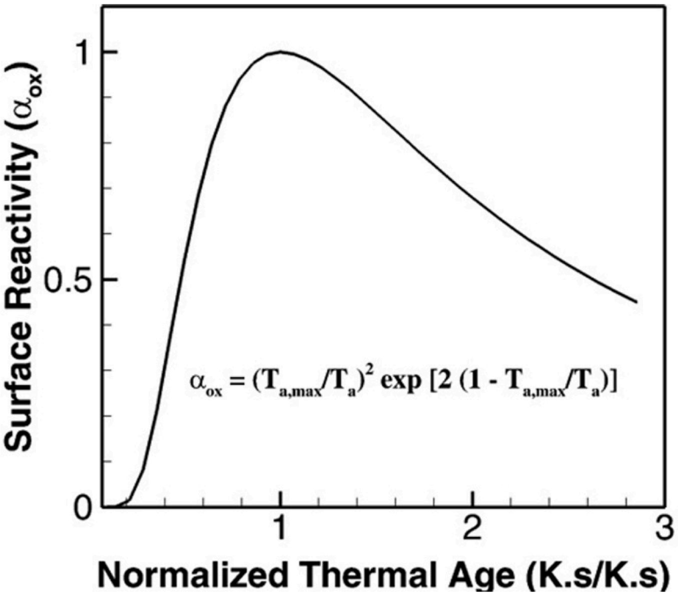

Figure 2.6. The parameter as a proposed function of normalized thermal age at the maximum soot concentration location [2].

This approach, which is referred to as the 'thermal age' model in this thesis, introduces the idea of incorporating the time-temperature history of the particle into the surface deactivation process. The thermal age considered in this approach assumes that the age factor is linear in both temperature and time which is not intuitively obvious as one would expect that the aging rate would be non-linear in temperature.

2.4 New Model Development

The previous section shows that all the present models are empirically developed, based on curve fitting both equations and parameters from the results of complex flames. Therefore, the development of a new soot surface aging model for the O_2 oxidation process which reflects the physics of the process is valuable. In this section, a new α model is introduced by adapting the coal char surface deactivation model [10] to employ it in modeling soot particle deactivation. The newly developed model is then calibrated with the data generated from the study of Pundle [5] before verifying with experimental data from the literature [7], [8].

As mentioned in Section 1.2.2, simulations of soot behavior involve two principal components: (1) gas-phase chemical kinetics, and (2) soot particle dynamics. In the present study, a detailed chemical kinetic model, The *FORCE* [25], is used to model the gas-phase chemical kinetics. This is coupling to the fluid dynamics via the standard flamelet model. The soot number density is then specifically solved by the fixed-pivot sectional method considering 30 fixed-pivot sections of soot particle volume with a spacing factor of (fs = vi+1/vi = 2) which covers the particle diameter range from 0.89 nm to 726 nm.

This study considers the nucleation, coagulation, surface growth, and oxidation processes. The nucleation process is defined as the dimerization of 2 pyrene molecules [14]. The coagulation process is modeled using the fixed-pivot sectional method [28], [31]. The surface growth is based on the widely used H-abstraction-C_2H_2-addition mechanism (HACA) [1], [14]. The main soot oxidizers are O_2 and OH which have different mechanisms [2]. The OH oxidation in this study follows Neoh's work which is based on collision efficiency [23], [32]. Soot oxidation by O_2 is initially modeled based on Appel, Bockhorn, and Frenklach (ABF)'s work [1] which can be written as,

$$R_{ox,O2} = \alpha k_5 [O_2][C_{soot^\circ}] \tag{1.15}$$

where the reader can refer to Section 1.2.2 for a description of the parameters.

As mentioned in Section 2.2, the oxidation of coal char presents many parallels to the oxidation of soot. Both fundamentally involve the interaction of oxygen with a carbon surface, and both have shown surface deactivation due to thermal aging [10], [39], [40]. More detail on the char surface thermodeactivation model can be found in Section 2.2. It is clear that ξ from [10] can be related to the soot α parameter via:

$$\xi = 1 - \alpha \tag{2.10}$$

By substituting Eq. (2.10) into Eq. (2.3) and maintaining n = 6.5 as it is originally used in [10], an equation for α can be developed:

$$\alpha = (\frac{\int_0^t k(T_{HT})dt}{0.181818} + 1)^{-1/5.5} \tag{2.11}$$

where $\int_0^t k(T_{HT})dt$ is called "soot age" and $k(T_{HT})$ is the thermodeactivation rate constant defined as follows:

$$k(T_{HT}) = A_d \exp\,(-\frac{E_d}{RT}) \tag{2.12}$$

The parameters A_d and E_d were initially adopted from the char literature [10]. The value of E_d was then adjusted to provide a match between emission data that were generated in previous experiments [5]. The model, with the modified value of E_d, was then used to predict the in-flame soot concentrations measured in two turbulent ethylene-air diffusion flames from the literature.

The calibration experiment is from the work of Pundle [5]. In brief, an ethylene-air non-premixed flame is established via an ethylene jet of diameter 2.18 mm at 47 m/s. The flame impinges on a surface normal to the axial flow that is 245 mm above the jet exit. The surface is held at 373 K. The exhaust gas is drawn through the hood from which some of the flow is tapped and diluted before the emission is measured by a tapered element oscillating microbalance (TEOM). By knowing the flowrate and the dilution ratio, a calculation of the total soot emission from the flame can be performed. More detail on the experiment is provided in Section 3.2 of this document. A schematic of the experimental equipment is shown in Figure 2.7.

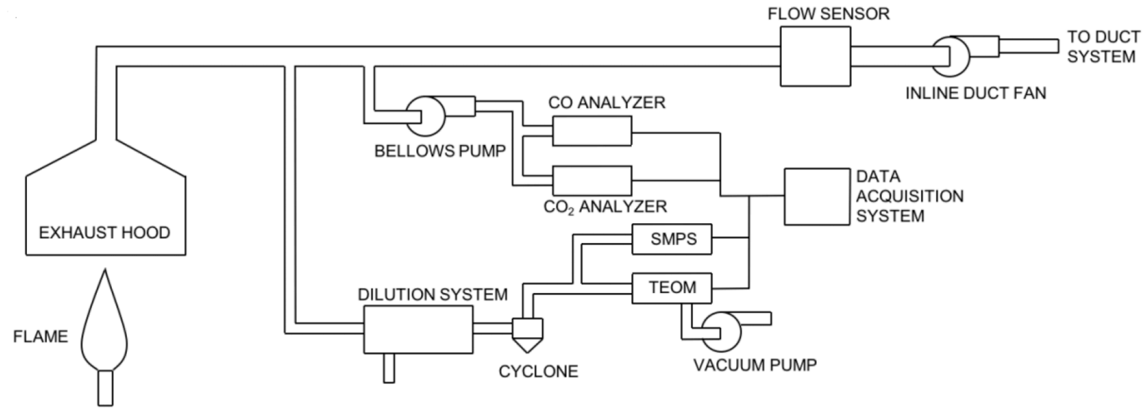

Figure 2.7 The detailed schematic diagram of the emission monitoring system [4].

The experimental results were compared against model results. The soot emission factor (mg/min) is obtained via a cross-sectional surface integration:

$$soot\ emission\ factor = \int f_v \rho_{soot} v_{axial} dA \qquad (2.13)$$

where f_v is the soot volume fraction, ρ_{soot} is soot particle density which is 1.8×10^9 mg/m^3, and v_{axial} (m/min) is the local axial velocity of the flow.

A sensitivity analysis of A_d and E_d on soot emission was conducted. The soot emissions are found to be significantly more sensitive to E_d. Figure 2.8 shows a plot of the emission factor for several E_d values with the dashed line representing the emission factor from the experiment (22 mg/min) [5].

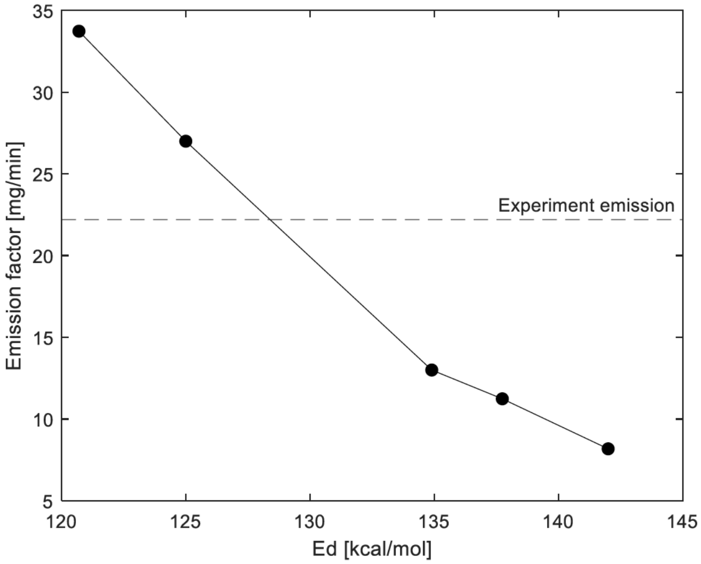

Figure 2.8 Emission factor plot versus E_d (solid line) with the emission factor from the experiment (dashed line) [5].

The results from Figure 2.8 suggest that the value of $E_d = 127.8$ kcal/mol leads to an agreement between the data and the model. This represents a 10% reduction from the value reported in the original literature for coal char. A summary of the model parameters is presented in Table 2.2.

Table 2.2

Thermodeactivation model parameters for char [10] and soot

Parameter	Char thermodeactivation model	Soot thermodeactivation model
A_d (s^{-1})	4×10^{21}	4×10^{21}
E_d (kcal/mol)	142	127.8
n	6.5	6.5

The final model is referred to as the soot thermodeactivation alpha model in this study.

2.5 Results and Discussion

The first validation study involves a laminar premixed flame. This experiment is presented by Xu et al. [6] on a fuel-rich premixed one-dimensional ethylene/air flame. The [C]/[O] ratio was 0.88 at 1 bar pressure with a cold gas burner velocity of 6.5 cm/s. The soot volume fraction was measured at various axial distances above the burner. This flame is referred to as XSF1.88 in this study. Due to the fact that the O_2 oxidation process is insignificant in this fuel-rich flame (see Figure 2.9), this flame is used to test the soot prediction performance of other processes within the model (nucleation, surface growth, coagulation, and OH oxidation).

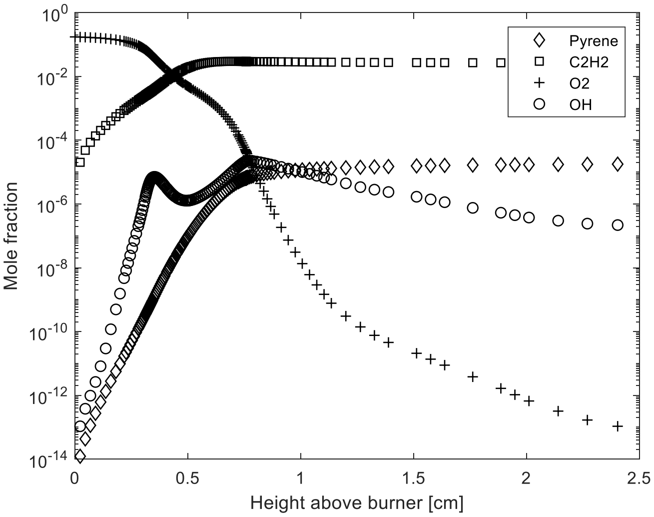

Figure 2.9 Species mole fraction plot for flame XSF1.88.

Soot formation in the XSF1.88 flame is modeled by first calculating the gas-phase species concentrations based on the temperature profile obtained from the experiment [6] with Appel, Bockhorn, and Frenklach (ABF)'s α model for the surface growth process [1]. The gas-phase species concentrations are then used to calculate the soot volume fraction via the fixed-pivot sectional method model mentioned previously. Regardless of the O_2 oxidation alpha model employed, the soot volume fraction plot remains unchanged and shows good agreement with the experimental data [6] as illustrated in Figure 2.10. This demonstrates that nucleation, surface growth, coagulation, and OH oxidation are well modeled in a system where O_2 oxidation is suppressed.

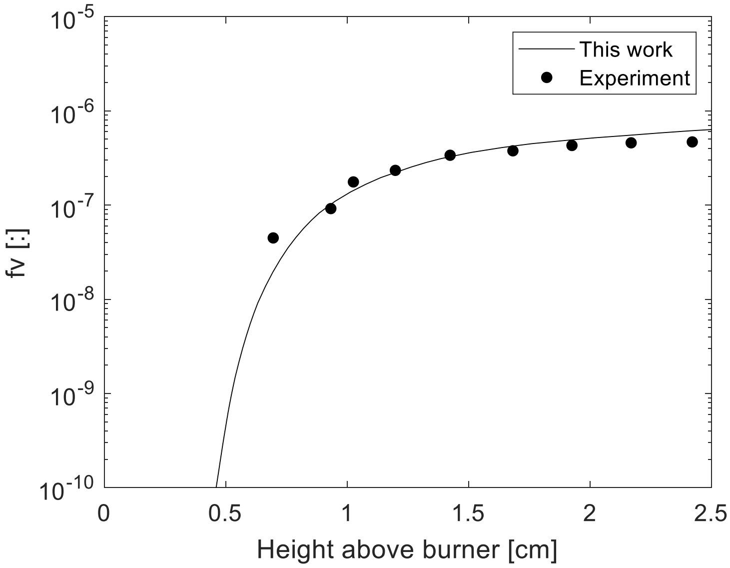

Figure 2.10 Predicted soot volume fraction plot for flame XSF1.88 against data from [6].

Two ethylene/air turbulent diffusion flames are modeled in the present study. These are the experiments of (1) Kent et al. [7] and (2) Young et al. [8]. In the first flame, the ethylene jet is preheated to 49 ºC and is injected through a 3 mm diameter nozzle at 52 m/s into a still air environment [7]. The second flame uses a 24.5 m/s ethylene jet at room temperature through a 3.1 mm diameter nozzle into atmospheric air. Soot volume fractions were measured both radially and axially at various axial and radial locations using optical diagnostics.

The present soot thermodeactivation model was applied to these two turbulent diffusion flames along with the literature models for α described in Section 2.2. These results are shown in Figures 2.11 and 2.12.

a)

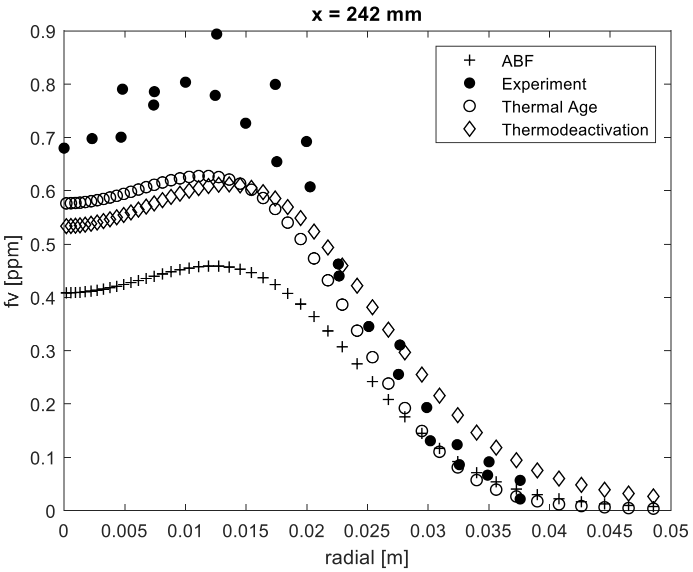

b)

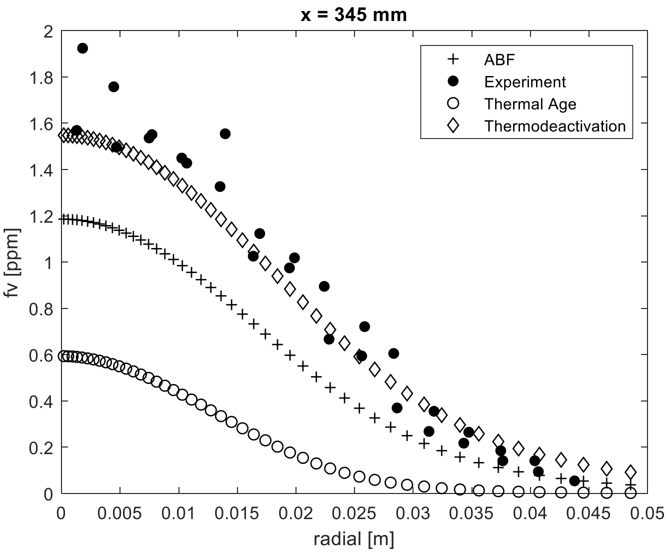

c)

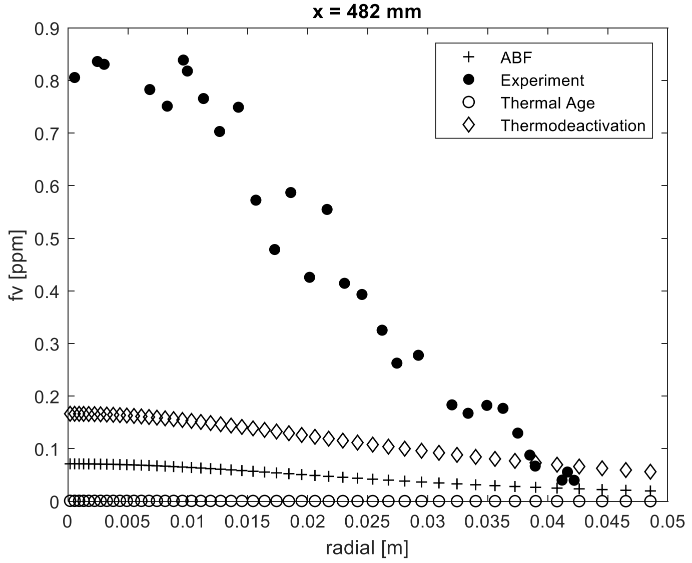

d)

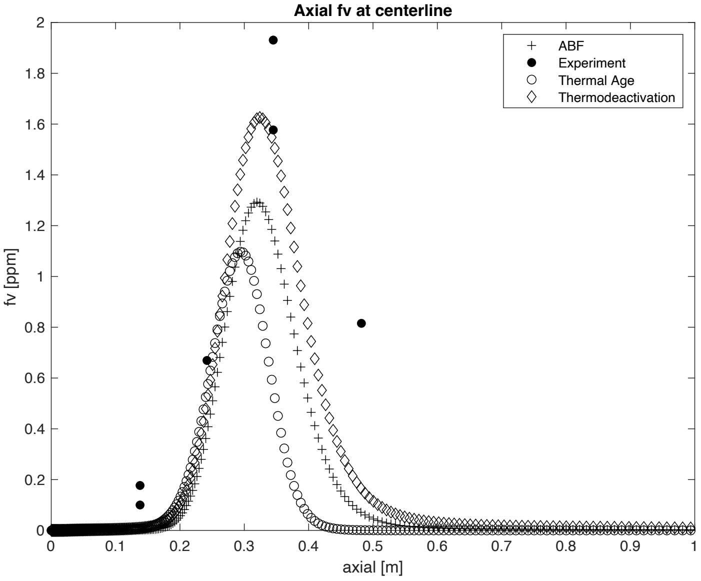

Figure 2.11 Volume fraction plot for a) radial variation at x = 242 mm, b) radial variation at x = 345 mm, c) radial variation at x = 482 mm and d) axial variation along the centerline against data from [7].

Figure 2.11 demonstrates the ability of the soot thermodeactivation model to predict soot formation in the flame from Kent et al. [7] compared with the ABF model and the thermal age model. The soot thermodeactivation model and the thermal age model yield good agreement in soot prediction in the early flame region (x = 242 mm). However, the calculated soot volume fractions from the thermal age model drop more quickly at an earlier location than other models resulting in an underprediction of soot for the later flame region. Using the ABF model produces a better prediction in the later flame region (x = 345 mm), nevertheless, soot is underpredicted throughout the flame. In a near post-flame region (x = 482 mm), all three models underpredict the data. The results for the new soot thermodeactivation model are, however, the closest to the data.

a)

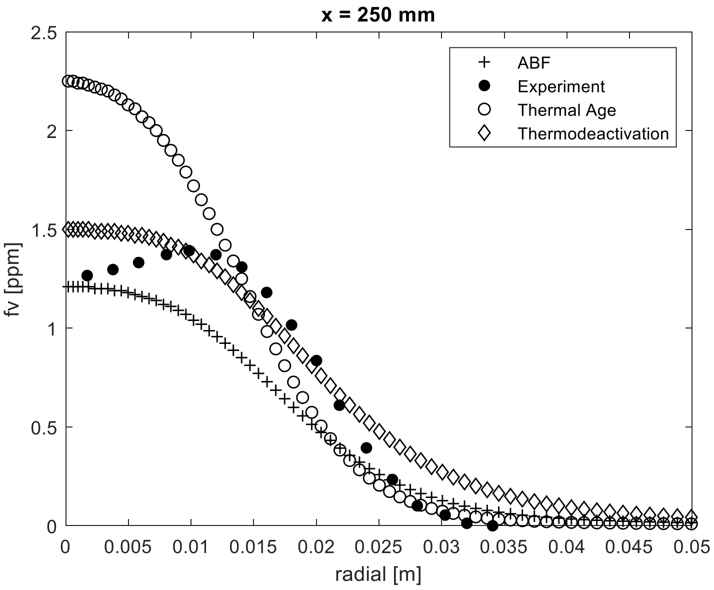

b)

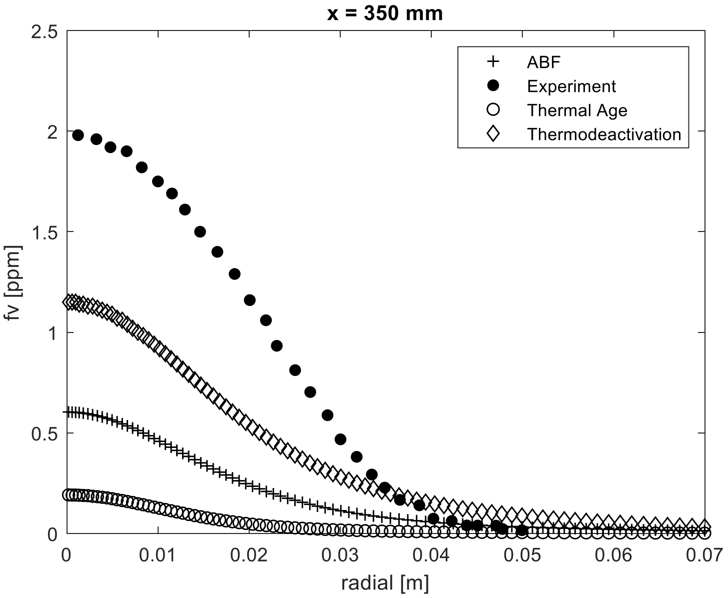

c)

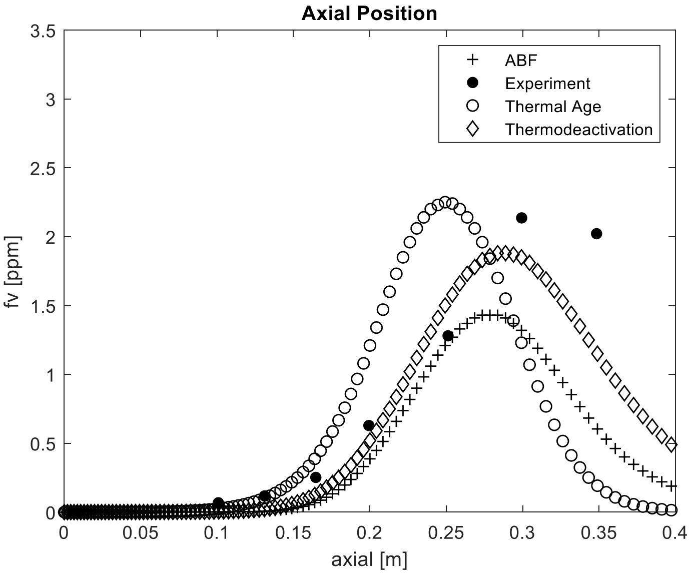

Figure 2.12 Volume fraction plot for a) radial variation at x = 250 mm, b) radial variation at x = 350 mm and c) axial variation along centerline against the data from [8].

Soot model predictions for the flame of Young et al. [8] are shown in Figure 2.12. A similar trend with those shown in Figure 2.11 is observed in which the thermal age model underpredicts the results at an earlier axial location compared to the other models. Underpredicted results are found in the later flame region for all models, however, the soot thermodeactivation model best matches the experimental data.

From the discussion above, it can be clearly seen that the new soot thermodeactivation α model predicts more accurate results than the current models for the flames studied [7], [8]. Apart from an improvement in the results, it is important to note that the new soot thermodeactivation alpha model developed in this study introduces a new means to model the soot surface aging process that follows the Arrhenius-type equation in which the rate of the process is non-linear in temperature. This soot thermodeactivation model is anticipated to have a better opportunity to accurately extrapolate to predict soot formation in a broader range of flames than empirically-based models.

The model of this work could be further improved by optimizing parameters against the pure soot O_2 oxidation experimental data. However, it is challenging to define the initial reactivity of the soot particle surface as the aging process must occur during the manufacturing of soot particles due to the surface growth process.

Chapter 3

Modeling of Soot Formation in Flames Impinging on a Cold Surface Part I

3.1 Overview

As mentioned in Chapter 1, 42% of the world's population still relies on biomass stove cooking according to the World Health Organization [11]. Emission reduction for biomass cookstoves has been an active research topic for a decade. One finding is that the emission of soot increases substantially when the flame impinges on the bottom of the pot [5]. To better understand this observation, Pundle and coworkers experimentally investigated the soot emission behavior of turbulent ethylene/air non-premixed flames impinging on a cold surface [5]. This study showed that the soot emissions increased when the flame impinged on the cold surface. These datasets provided quantitative soot emission information as a function of the distance between the jet nozzle and the cold surface. The objective of the work reported in this chapter is to understand the mechanism giving rise to this enhanced emission through the use of the dynamic soot model developed and described in the previous chapter. This chapter starts with a description of the experimental work reported by Pundle [5]. The results of simulations with three different soot surface aging models (i.e., the ABF model, the thermal age model, and the soot thermodeactivation model) are presented. The influence of the presence of a cold surface at a different location in the flame is studied. Finally, the relative contributions of thermal quench versus fluid dynamic strain are explored by comparing the results for a flame impinging on a cold surface versus a flame impinging on an adiabatic surface.

3.2 Literature Review

This section provides an overview of the experimental work of Pundle and coworkers [5]. Ethylene is the fuel most commonly used for diffusion flame soot studies [4], so it was adopted for their work by Pundle et al. [5]. The extensive literature on free jet flames provides an excellent point of comparison with flames impinging on a cold surface (a configuration not previously reported in the literature). During all experiments, the temperature of the cold stainless-steel round disk was maintained at 373 K by the presence of boiling water on the opposite side. In the experiment, the 99.95% ethylene stream was injected through nozzles of various diameters into quiescent air at ambient temperature. The exhaust gas was drawn at a constant velocity of 0.08 m/s through the hood by an axial flow fan. In the exhaust line, concentrations of CO and CO_2 were also measured. Soot mass in the exhaust flow was measured in real-time by a Tapered Element Oscillating Microbalance (TEOM). Such a system relies on the fact that the change of mass on the filter alters the natural frequency of the oscillation. More detail on the TEOM is provided elsewhere [4]. Since the TEOM is generally designed for measuring ambient emission, a dilution system was introduced to this high-emission experiment. The particle size distribution was also measured in this work by Scanning Mobility Particle Sizer (SMPS) technique. The detailed schematic diagram of the system is shown in Figure 3.1.

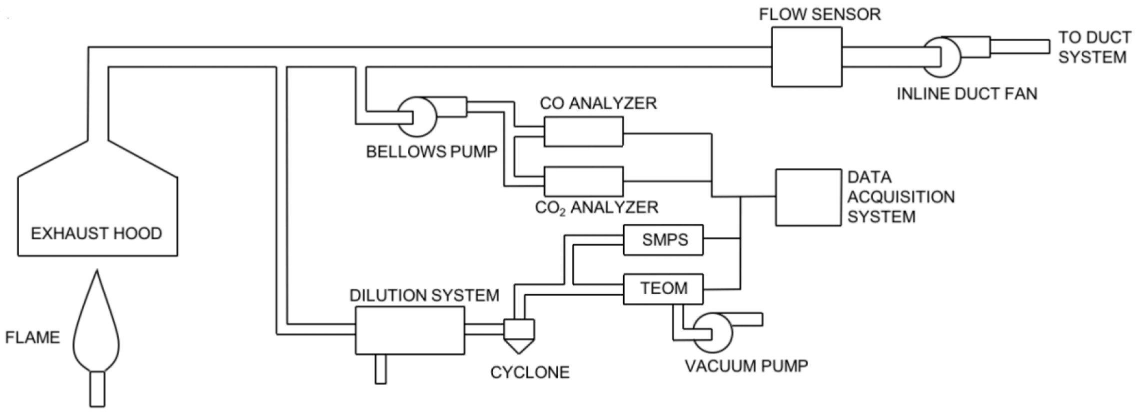

Figure 3.1 The detailed schematic diagram of the emission monitoring system [4].

In the study, several free-flame configurations were studied which were implemented by varying the fuel nozzle diameter and fuel velocity. Four different nozzles are used with inner diameters of 1.5 mm, 2.18 mm, 3 mm, and 4.5 mm. The fuel jet velocity was varied in the range from 6 m/s to 80 m/s [5]. A summary of all the flame conditions is provided in Table 3.1.

Table 3.1

Summary of Flame Conditions [5]

Flame	Nozzle diameter (mm)	Jet Velocity (m/s)	Heat Output (kW)	Jet Reynolds number	Flame Length (mm)	Liftoff (mm)	Richardson's ratio	Jet Strain rate
A	1.5	50	5	8300	0.410	12	120	33320
B	1.5	60	6	10000	0.430	19	90	39990
C	1.5	70	7	11500	0.440	26	70	46650
D	1.5	80	8	13200	0.450	32	60	53320
E	2.18	30	6	7200	0.480	8	240	13760
F	2.18	40	8	9600	0.520	10	180	18330
G	2.18	47	9	11300	0.570	16	160	21550
H	2.18	60	12	14400	0.600	31	120	27530
I	3	25	10	8300	0.570	4	330	8330
J	3	30	11	10000	0.630	9	280	10010
K	3	35	13	11500	0.640	12	250	11660
L	3	40	15	13200	0.700	15	220	13330
M	3	52	20	17200	0.760	26	170	17330
N	4.5	6	5	3000	0.470	0	1280	1330
O	4.5	8	7	4200	0.550	0	960	1890
P	4.5	15	13	7400	0.648	0	610	3330
Q	4.5	20	17	10000	0.741	0	480	4440

A subset of these free flames was impinged on a cold surface, with the principal variable being the distance between the nozzle exit and the cold surface. The soot emissions from each experiment are measured in units of mg_{soot}/min. The measured emission is then normalized by the carbon input resulting in a non-dimensional parameter called soot yield factor, χ_s,

$$\chi_s = \frac{\dot{m}_{soot}}{\dot{m}_C} \tag{3.1}$$

where $\dot{m}_{soot}$ is the mass flow rate of emitted soot, and $\dot{m}_C$ is the mass flow rate of carbon in the fuel stream [5]. The results for flames E, F, G, and H are shown in Figure 3.2 as a plot of the soot yield factors versus a non-dimensional height, $h*$, which can be expressed as,

$$h^* = \frac{h}{L_f} \tag{3.2}$$

where h represents the distance between a cold surface and burner, and L_f is the nominal free flame length.

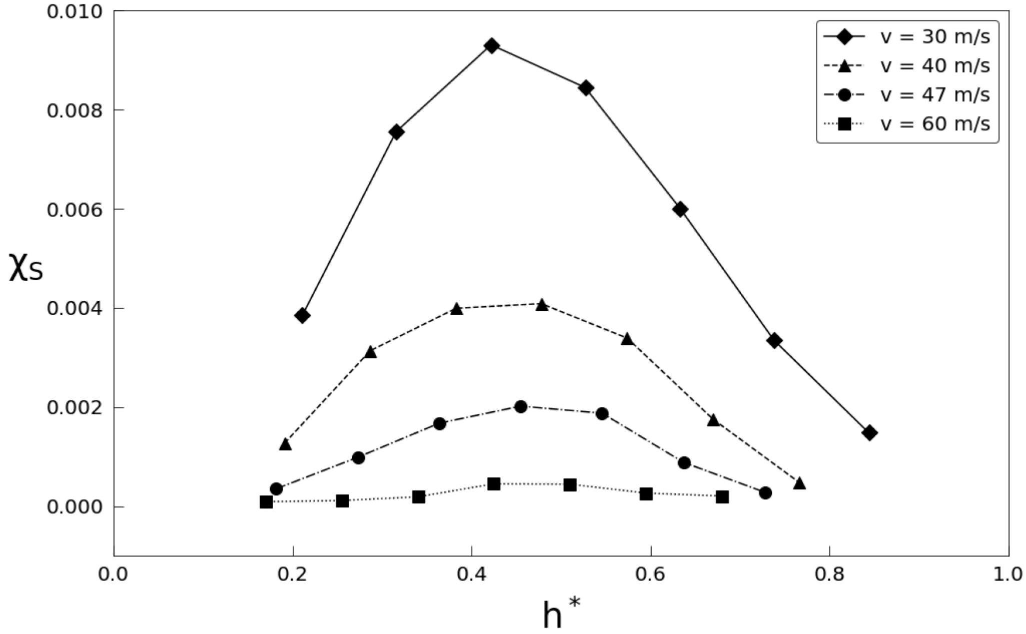

Figure 3.2 Plot of soot yield factors of flames E, F, G, and H impinging on a cold surface at different values of non-dimensional height h^* [5].

Since all the flames reported in Figure 3.2 used the same jet diameter, the figure suggests that increasing the jet velocity reduces soot emission. Furthermore, all the flames tended to produce their maximum soot emission at around the same value of $h^*=0.5$. The author speculated that at low h^*, the presence of the cold surface suppresses nucleation by attenuating PAH formation as temperature decreases due to more heat loss to the cold surface [5]. This eventually reduces the number of new particles created by the initial nucleation event. Placing a cold surface in a low h^* region also restrains the surface growth process by hindering the formation of C_2H_2 which is the main precursor for soot formation [5]. At larger h^* values, nucleation is enhanced, producing more sites for the surface growth process. Moreover, the cold surface also inhibits the soot oxidation process, resulting in more soot emission from the flame. At very high $h*$ values, the oxidation process is not suppressed as the cold surface is placed outside the oxidation zone resulting in lower soot emission [5]. The author also claimed that the entire dataset gives the mean for maximum soot emission at $h* = 0.46$ which corresponds with the location of maximum soot volume fraction in the ethylene/air turbulent diffusion flames reported by Kent [7]. These mechanistic speculations are what we seek to investigate via modeling.

3.3 Model Development

The domain of the model is designed to match the experiment [3]. This is an axisymmetric turbulent non-premixed flame impinging on the cold surface (a pot containing boiling water). The fuel inlet at the bottom introduces a vertical flow of ethylene at 300 K into the quiescent air at 300 K through a 2.18-mm nozzle with a velocity of 47 m/s. A 240-mm diameter cookpot with 140-mm height with a constant temperature of 373 K (boiling point of water) is introduced in the simulation to reflect the experiment. The distance between the bottom surface of the pot and the fuel nozzle is varied, which including values of 150 mm, 200 mm, 245 mm, and 300 mm. The simulation model schematic is shown in Figure 3.3.

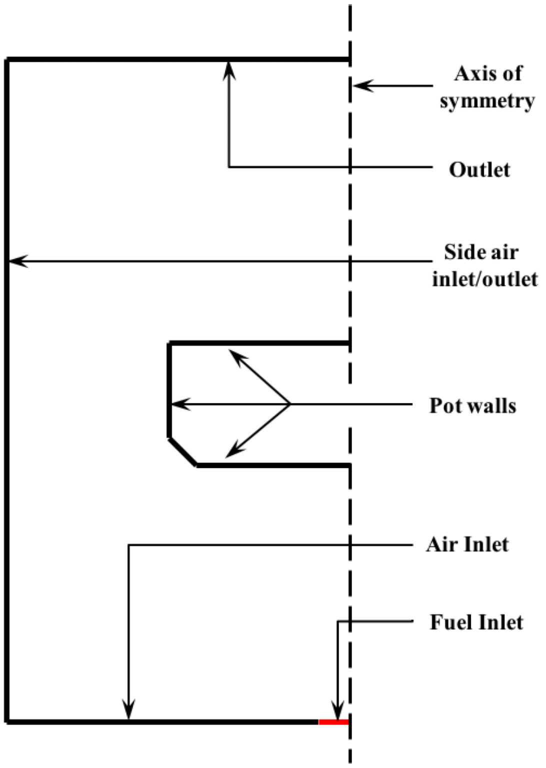

Figure 3.3 Schematic of the computational domain [5].

As discussed in Chapter 2, the simulation solves the conservation equations for mass, momentum, and energy using the Reynolds Average Navier-Stokes Equations (RANS) approach. Since this simulation includes both the near-wall flow and free flow, the Shear Stress Transport k-ω (SST k-ω) model is used. This solves transport equations for turbulent kinetic energy (k) and the specific turbulent dissipation rate (ω). Such a model is the combination between the k- ω model and the k- ε model. The k- ω model is generally used to simulate the boundary layer flow in the near-wall region, while the k-ε is known to yield a good result in free-flow simulation. Therefore, a blending function is inserted into the SST k-ω model in a way that the model employs the k-ε model in the region far away from the surface and gradually introduces the k-ω model for the fluid close to the surface.

The calculation of turbulence adjacent to the surface is purely controlled by the k- ω model. More detail of the SST k-ω model is discussed elsewhere [44]. As mentioned in Section 2.4, the flamelet model is employed to handle the interaction between the turbulence and the combustion chemistry. This assumes that the turbulent diffusion flame consists of thin, laminar, one-dimensional counter-flow flamelet structures which can be described by two quantities, the mixture fraction, f, and the scalar dissipation rate, χ [45] (i.e., a local stoichiometry and a fluid strain rate). Therefore, the species mass fraction and temperature in a turbulent field can be parameterized by the mixture fraction and scalar dissipation as expressed,

$$\overline{\emptyset} = \int\int \emptyset(f,\chi)p(f,\chi)df d\chi \tag{3.3}$$

where $\emptyset$ is the species mass fraction and temperature. In this study, f and χ are assumed to be statistically independent which simplifies the joint PDF $p(f, \chi)$ to $p(\mathrm{f})p(\chi)$. The $p(\mathrm{f})$ is assumed to have a beta PDF shape while the $p(\chi)$ is assumed to be a delta function. As the transport equation of f and χ are solved, $\overline{\emptyset}$ can be determined. To reduce the calculation time, the values in Equation (3.3) for all species and temperature are precalculated and tabulated as a look-up table. More detail on the flamelet method can be found in [45].

As mentioned in Chapter 2, this study uses the detailed chemical kinetic mechanism developed by Blanquart et al. [25], *The FORCE*, which considers 192 species and 1896 chemical reactions including important PAH formation pathways which are essential to model the soot nucleation process. In the present study, the flamelet equations for the mass fraction of species and temperatures are solved for 30 different values of the scalar dissipation rate ranges from 10^{-3} s^{-1} to 192 s^{-1}. The calculated flamelets are then convoluted with the joint PDFs of mixture fraction and scalar dissipation rate in Equation (3.3) yielding the precalculated look-up table for the mean species mass fraction and the mean temperature as a function of mixture fraction, scalar dissipation rate, and the mean enthalpy. As f, χ, and $\overline{H}$ are determined from the flowfield, the average species mass fraction and the average temperature can then be obtained.

In this study, the dynamic viscosity is assumed to follow Sutherland's law [46]. The gas mixture thermal conductivity is set to be a polynomial function of reduced temperature [47]. Each specie is also assumed to have a temperature polynomial functional form of specific heat constant. To calculate the turbulent viscosity, a value of 0.9 is employed for the turbulent Schmidt number.

A brief description of the soot model employed in the simulation is provided here for the reader's convenience. More detail on the soot model can be found in Section 1.2. The soot particle size distribution function (PSDF) is modeled by the widely-used fixed-pivot sectional method [28], [31] to solve the population balance equation (PBE). By using this technique, particles in each size section are assumed to have a unique representative size which significantly simplifies the calculation process. The PBE of the k^{th} size pivot of the N pivots takes the form of a single-phase flow scalar transport equation with source/sink term included [45],

$$\frac{\partial \rho \phi_k}{\partial t} + \frac{\partial}{\partial x_i}\left(\rho u_i \phi_k - \mathcal{D}\frac{\partial \phi_k}{\partial x_i}\right) = S_{\phi_k}, k = 1, \dots, N \qquad (3.4)$$

where ϕ_k is the number density of soot particle in the k^{th} pivot, ρ is the gas density, u_i is the advective velocity, $\mathcal{D}$ is the soot diffusivity which considers the effect of both molecular and turbulent diffusivities of soot, and S_{ϕ_k} is the source/sink term of the number density in the k^{th} pivot. Terms on the left-hand side of Equation (3.4) are related to the flowfield. The soot number density source/sink term, S_{ϕ_k}, on the right-hand side is, however, the result of the soot formation processes. In this work, the nucleation process is modeled using the pyrene dimerization approach [14]. Surface growth is modeled to follow the well-known HACA mechanism with the ABF α model [1]. Coagulation is simulated based on the fixed-pivot sectional method proposed by Kumar et al. [31]. Soot oxidation by OH is calculated by adopting the theory of collision between OH radical and soot particle from Neoh and coworkers [23]. Finally, the oxidation by O_2 is modeled based on the work of Nagle Strickland-Constable [22]. The surface aging model used for O_2 oxidation follows the soot thermodeactivation model which is developed in Chapter 2 of this work. All the reaction rates can be found in Table 1.1. Similar to Chapter 2, the geometric spacing factor of 2 ($f_s = 2$) between pivots is employed with 30 fixed-pivot sections of soot particle volume considered covering the particle diameter range from 0.89 nm to 726 nm.

Several studies report that the presence of soot strongly affects the temperature field, mainly because of the emission of radiation from the soot particles. Therefore, employing a suitable radiation model is essential for a simulation of soot in the flame. In this study, the Discrete Ordinates (DO) Method is used. In such a method, the Radiative Transfer Equation (RTE) is solved for a finite number of solid angels in $\vec{s}$ direction,

$$\nabla \cdot (I\vec{s}) + (a + \sigma_s)I = a\frac{\sigma T^4}{\pi} + \frac{\sigma_s}{4\pi}\int_0^{4\pi} I d\Omega \qquad (3.5)$$

where *I* represents the radiation intensity, a is the absorption coefficient, σ_s is the scattering coefficient, σ is the Stephan-Boltzmann constant which has a value of 5.67×10^{-8} $Js^{-1}m^{-2}K^{-4}$, and Ω represents the solid angle [45]. In the present work, the soot particle absorption coefficient is calculated by the widely-used function proposed by Sazhin et al. [48] which can be expressed as,

$$a_{soot} = B \cdot \rho_{soot} f_v (1 + C(T - 2000)) \qquad (3.6)$$

where B = 1232.4 m^2/kg, $C = 4.8\times10^{-4}$ K^{-1}, T is the temperature (K), and f_v is the soot volume fraction. The soot volume fraction can be obtained via:

$$f_v = \sum_{i=1}^{N} N_i V_i \qquad (3.7)$$

where N is the total number of the size pivots, N_i is the soot number density in the ith pivot with the unit of $\#/m^3$, and V_i is the volume in the ith pivot with the unit of m^3.

The solver employed in this work is the widely-used ANSYS Fluent package. The finite volume technique is used to solve all equations with the pressure-based coupled algorithm, within which the momentum equations and the pressure-based continuity equation are solved simultaneously to provide more robustness [45]. The soot population balance equations are solved by a first-order upwind scheme while all other equations are solved by a second-order upwind scheme.

3.4 Results and Discussion

Calculated soot emission factors as a function of the nozzle-to-surface distance are illustrated in Figure 3.4.

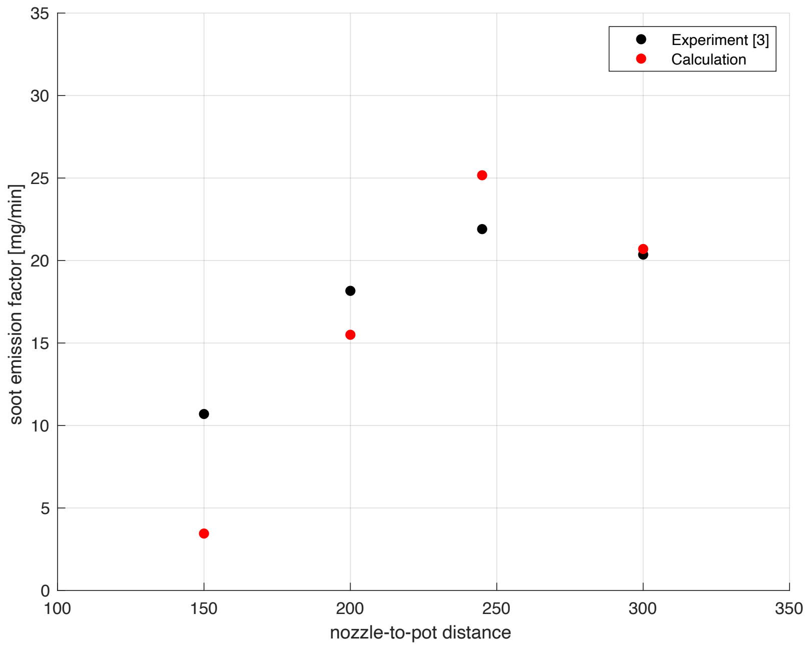

Figure 3.4 Plot of soot emission factor (mg/min) for all cases.

Figure 3.4 shows that the calculated emission factor increases as the pot is moved away from the nozzle and peaks at the distance of 245 mm before decreasing as the pot is moved further. This is consistent with the experimental data shown in the same plot. The goal is to identify the mechanistic reasons associated with this behavior.

Since the presence of the pot (filled with water) introduces a constant-temperature surface (373 K) boundary condition to the flame, quenching of the flame gases could potentially arrest soot oxidation, leading to enhanced emissions. One approach to evaluate this is to use the model to remove heat extraction as a process. This can be achieved by simulating an adiabatic pot surface, thus omitting all heat extraction by the pot surface. The results of the simulation are shown in Figure 3.5.

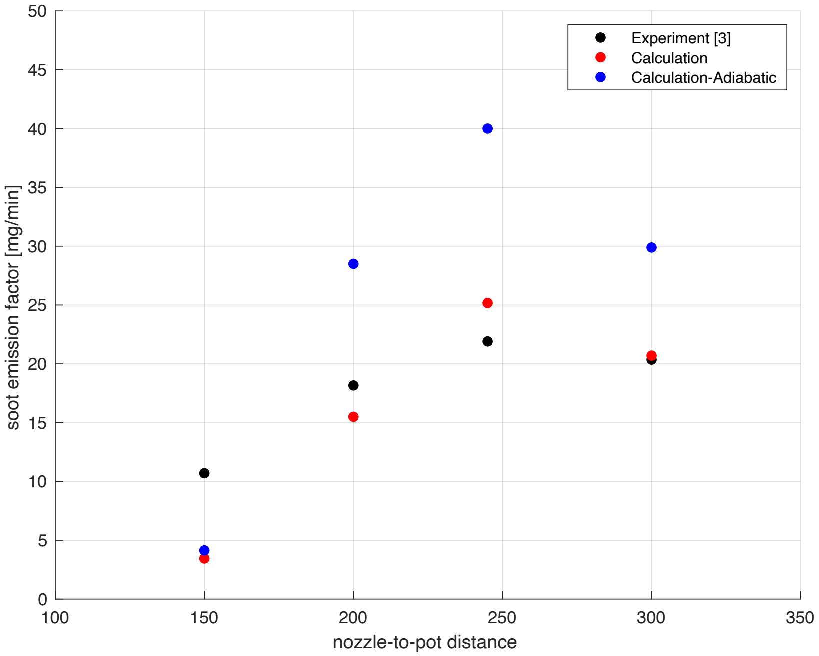

Figure 3.5 Calculated soot emission factor (mg/min) of non-adiabatic and adiabatic pot surface.

With the heat extraction eliminated, the soot emission factors are expected to be lower as the oxidation process is not quenched by heat transfer. Nevertheless, Figure 3.5 indicates the opposite. Therefore, it is possible that the change in the fluid flow patterns associated with the presence of the surface is an important mechanism influencing the emission.

Evaluating mechanisms involves examining in-flame behavior. An important tool in understanding in-flame behavior is the integrated soot flux, which can be calculated the same way as the soot emission factor in the flame region (Eqn. 2.13). In brief, the integrated soot flux is a surface integral of the product of the soot concentration and the local axial mass flux (the product of the velocity and the local density). This quantity represents the amount of soot at each sectional plane that is normal to the axis which contributes to the emission. Comparing the in-flame integrated soot flux between cases allow the influence of the presence of a surface on the in-flame soot volume fractions to be investigated. For comparison, the baseline case for the free flame (i.e., no surface) is included. Figure 3.6 shows the integrated soot flux for all the non-adiabatic surface cases along with the free flame.

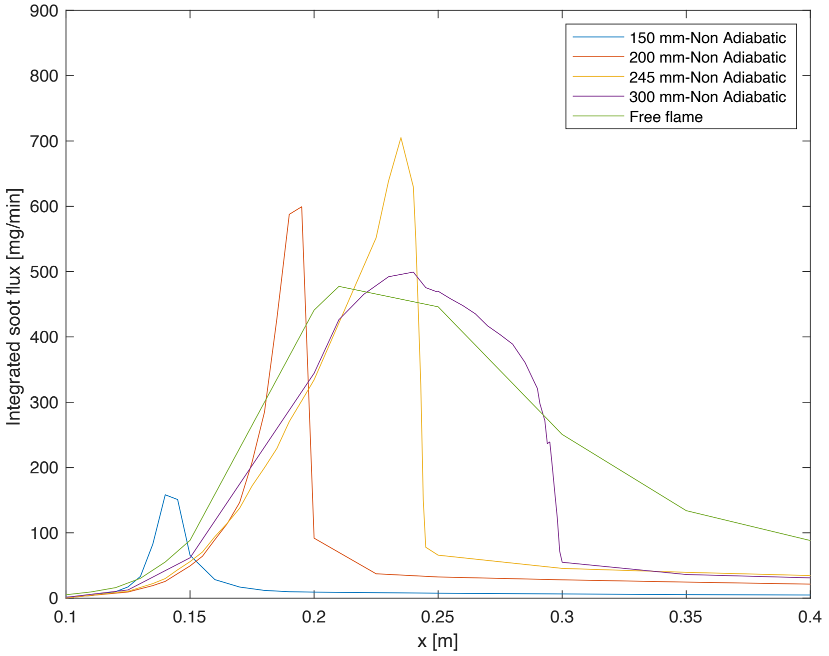

Figure 3.6 Calculated integrated soot flux (mg/min) of non-adiabatic pot surface cases and free flame case.

From Figure 3.6, peaks of integrated soot flux tend to always be in the region immediately upstream of the impingement surface. Thus, the peaks track the location of the surface as it is moved downstream. For 150-mm to 245-mm cases, the peak locates at the region close to the surfaces. However, for a 300-mm case, the integrated soot flux peaks at the location slightly upstream of the pot surface. All pot cases experience a sharp drop at the surface which is not observed from the free-flame case. At this point, it is logical to hypothesize that due to the presence of the surface, the flame is spread radially around the surface allowing more O_2 penetration into the flame which dramatically enhances the O_2 oxidation process.

The quantitative approach to prove this hypothesis is included in the scope of Chapter 4. To identify the influence of the temperature, simulations with the absence of heat transfer between the surface and the flame were conducted. The results are shown in Figure 3.7.

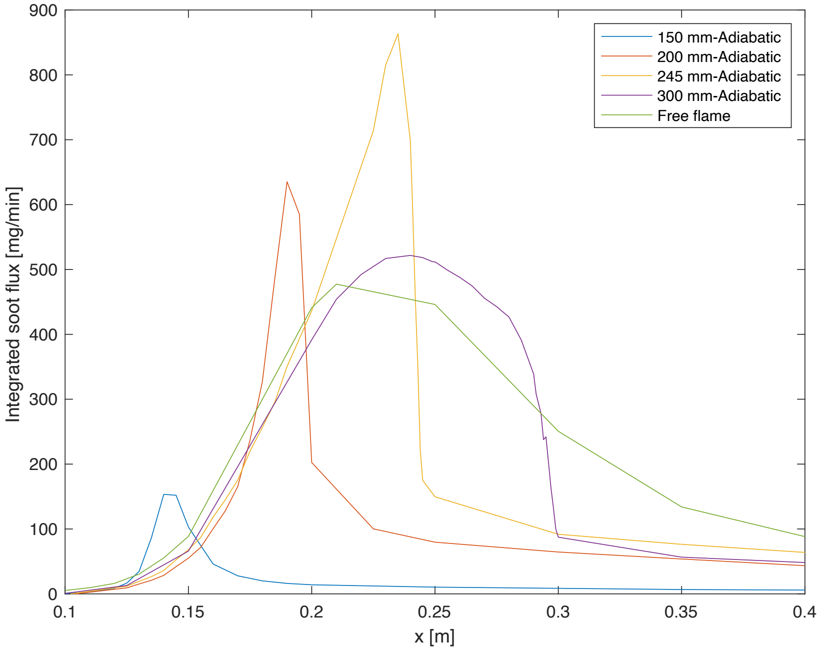

Figure 3.7 Calculated integrated soot flux (mg/min) of adiabatic pot surface cases and free flame case.

The same trend previously observed in Figure 3.6 is observed in Figure 3.7 in which the peak shifts downstream as the pot surface moves away from the nozzle. Also, the highest peak is found from 245-mm case. All cases still experience a sharp drop close to the surface as the flow field due to axial flow stagnation, similar to the non-adiabatic cases. Despite these similarities, the peaks of the integrated soot flux for the adiabatic cases are higher than the non-adiabatic cases.

At this point, the reason underlying this behavior has not yet been identified. One approach to resolving this is to examine the magnitude of the various source terms present in the conservation equations. Since the emission factor is the result of the sum of all the processes occurring throughout the domain, volume integration of each source term is proposed as qualitative means of identifying the contribution of the various processes to the overall behavior. Table 3.2 shows volume integration of all source terms for the cases of (1) the adiabatic pot surface, and (2) the corresponding free flame.

Table 3.2

Summary of volume integration source terms for adiabatic-surface and free-flame cases

Source term (kg/s)	150 mm	200 mm	245 mm	300 mm	Free flame
Nucleation	4.18E-8	1.5E-9	1.34E-9	1.29E-9	1.15E-9
Surface growth	1.49E-5	1.8E-5	2.24E-5	1.94E-5	1.74E-5
O_2 oxidation	-8.65E-6	-6.96E-6	-9.14E-6	-9.37E-6	-7.61E-6
OH oxidation	-3.79E-6	-5.45E-6	-6.78E-6	-5.25E-6	-4.21E-6

The table suggests that the enhancement of soot emissions when the adiabatic surface is present is not due to a reduction in the overall oxidation rate since oxidation is actually enhanced for those cases involving the surface. The striking feature is that the surface growth rate is (1) numerically the largest contributor to the creation of soot mass in all cases, and (2) it is the most enhanced by the presence of the surface. This is also supported by the fact that the in-flame integrated soot fluxes of the adiabatic cases are higher than the non-adiabatic cases, i.e., the absence of heat extraction leads to faster chemistry for all the processes. Of the two processes responsible for mass addition, nucleation and surface growth, the enhancement of the surface growth in the presence of the surface appears to dominate the higher soot volume fractions observed. Note that the case with the highest soot emission, the 245 mm surface height, corresponds to the highest surface growth value. Since the surface growth source term is based on the chemical reaction between the surface and C_2H_2, understanding the behavior of C_2H_2 for the various cases could help understand the overall soot behavior. In an approach similar to that used for the source terms, the volume-integrated C_2H_2 molar quantity for each case was calculated. Table 3.3 shows the kmoles of C_2H_2 present in each of the flames.

Table 3.3

Summary of volume integration of species concentration for adiabatic-surface and free-flame cases

Volume integration (kmol)	150 mm	200 mm	245 mm	300 mm	Free flame
C_2H_2	2.24E-8	2.36E-8	2.50E-8	2.51E-8	2.27E-8

According to Table 3.3, integrated C_2H_2 increases from 150-mm case to 245-mm, and 300-mm case before decreasing toward the free flame value. C_2H_2 of 245-mm and 300-mm cases are slightly different, nevertheless, the surface growth term is less in the case of 300 mm. Table 3.2 suggests that the O_2 oxidation is higher for the 300-mm case. A higher oxidation source term leads to less surface area for the 300-mm case resulting in a lower surface growth source term.

The question is then why the C_2H_2 kmoles respond to the presence of the surface in the manner suggested by Table 3.3. Since the phenomenon of increased C_2H_2 takes place with the surface in place, but in the absence of heat transfer to the surface, the suggestion is that the behavior originates in the change in fluid dynamics caused by the surface. To explore this, contour plots of C_2H_2 concentration were prepared for various surface heights in Figure 3.8.

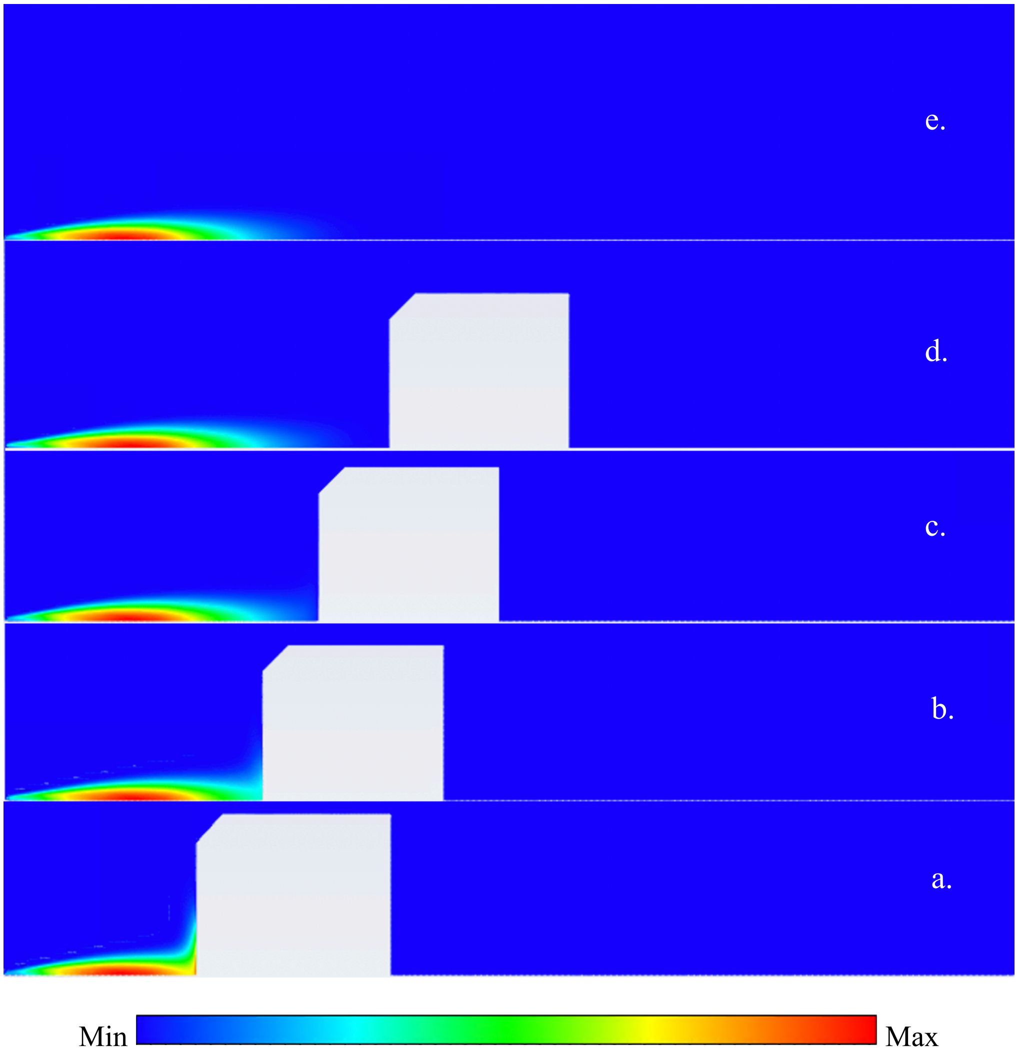

Figure 3.8 Contour plot of C_2H_2 mass fraction normalized by the maximum concentration of each case for the adiabatic surface cases and the free flame case which a) 150-mm case, b) 200-mm case, c) 245-mm case, d) 300-mm case, and e) free-flame case.

From Figure 3.8, the C_2H_2 concentration is at a maximum at the centerline for all cases, making the centerline an area of interest for studying C_2H_2 behavior during the interaction of the jet with the surface. Note that the C_2H_2 spatial concentration variation does not change significantly until the surface directly interacts with the flow. The action of the surface appears to spread the C_2H_2 out. Since there is no heat transfer to the pot surface, the changes taking place are in response to changes in the fluid dynamics. The impingement of the jet on the surface could be expected to lead to changes in mixing, which would influence both the stoichiometry and the shear experienced by the fluid. Both of these are important parameters in the flamelet model used for the chemistry, so both could influence the C_2H_2.

In the flamelet model, the chemistry is parameterized against (1) the mixture fraction (f , an analog for stoichiometry), and (2) the scalar dissipation (χ, an analog for local strain rate,). The approach is to:

1. See whether the presence of the surface significantly changes either of these two parameters, and
2. See whether the changes in these parameters influence C_2H_2 concentrations in a way that rationalizes the results.

Figure 3.9 illustrates the variation of mixture fraction along the centerline for 150-mm, 245-mm, and free-flame cases. These 3 cases are chosen as they should represent the variation of all cases.

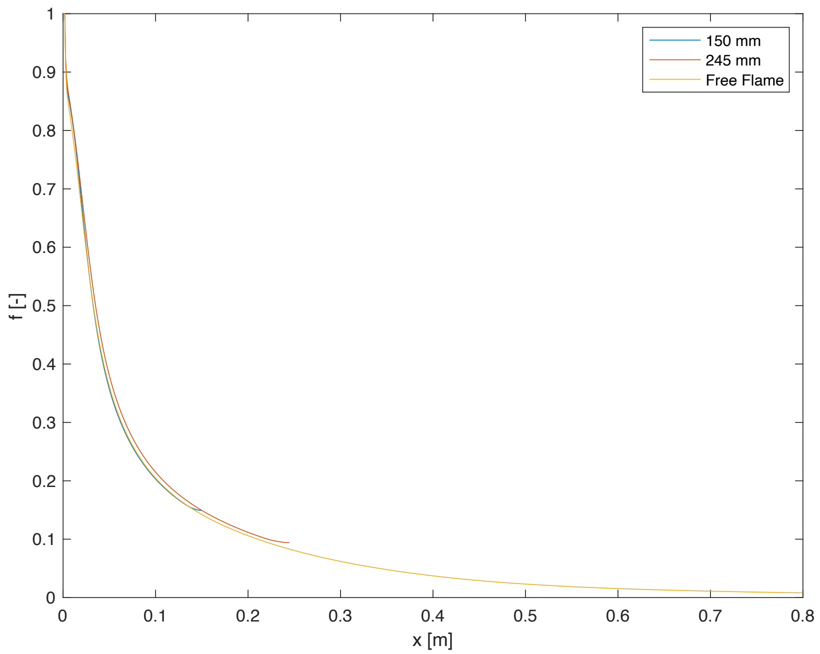

Figure 3.9 Plot of the centerline mixture fraction of 150-mm adiabatic surface, 245-mm adiabatic surface, and free flame case.

Figure 3.9 shows that the centerline mixture fraction values are all similar right up to the surface. Therefore, the attention turns to the influence of the scalar dissipation rate on C_2H_2. A specific range of the mixture fraction is required to study the relationship between the C_2H_2 concentration and the scalar dissipation rate. One approach is to investigate the variation of C_2H_2 concentration with *f* which is shown in Figure 3.10.

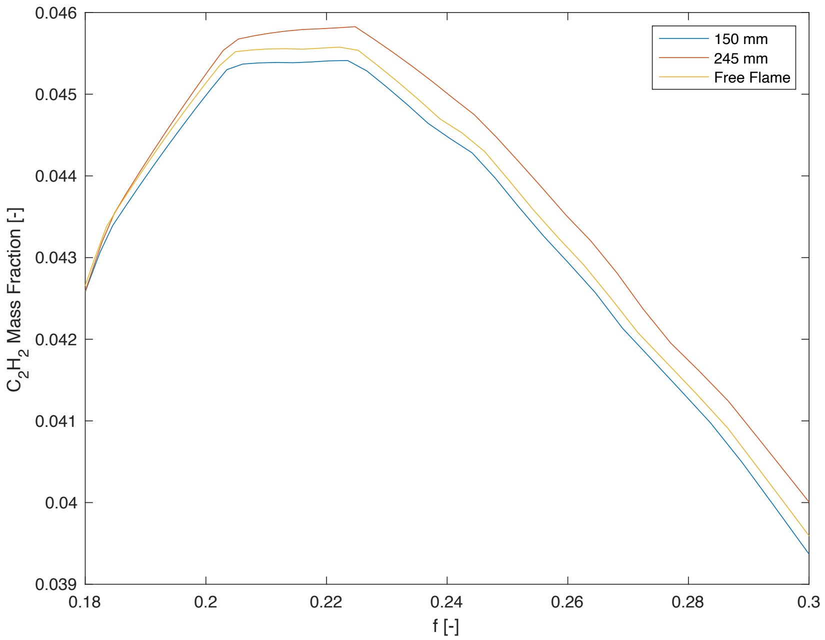

Figure 3.10 Variation of the C_2H_2 mass fraction against the centerline mixture fraction for 150-mm, 245-mm, and 300-mm cases.

Figure 3.10 correlates the C_2H_2 mass fraction against the mixture fraction on the centerline for three of the cases (two with surface impingement plus free flame). The behavior with mixture fraction is remarkably similar for all three cases, showing that C_2H_2 mass fraction tends to peak between 0.2 to 0.23 for all cases. We now fix the mixture fraction and look at how C_2H_2 varies with scalar dissipation, as presented in Figure 3.11.

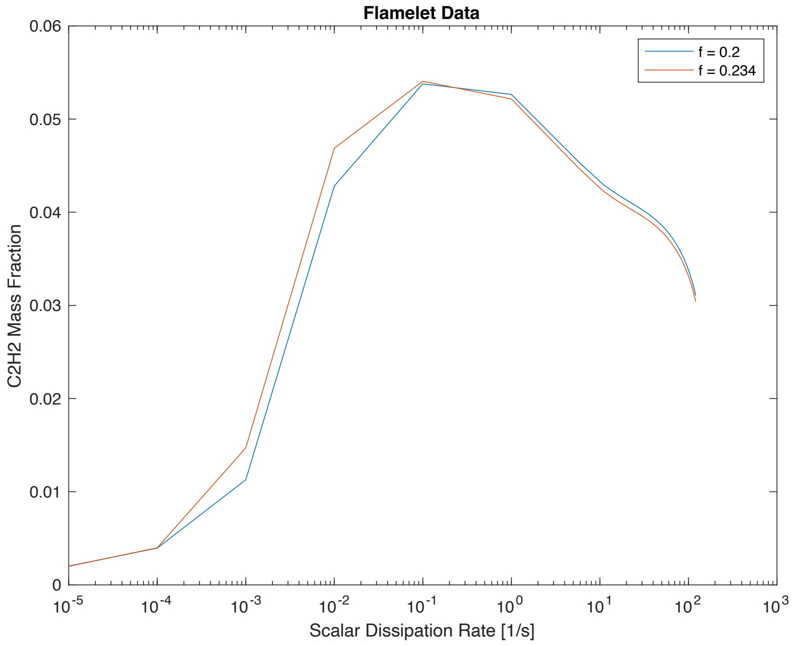

Figure 3.11 Variation of C_2H_2 mass fraction along scalar dissipation rate for f = 0.2, 0.234, and 0.27.

Figure 3.11 shows that C_2H_2 does indeed change substantially with scalar dissipation. It also shows (similar to Figure 3.10) that at a fixed value of scalar dissipation, the C_2H_2 is insensitive to mixture fraction at values that are representative of the centerline environment. Since C_2H_2 responds to local strain rate, the next step is to examine how the presence of the surface changes the scalar dissipation and local strain rate. Figure 3.12 shows a plot of the scalar dissipation rate of all cases along the centerline.

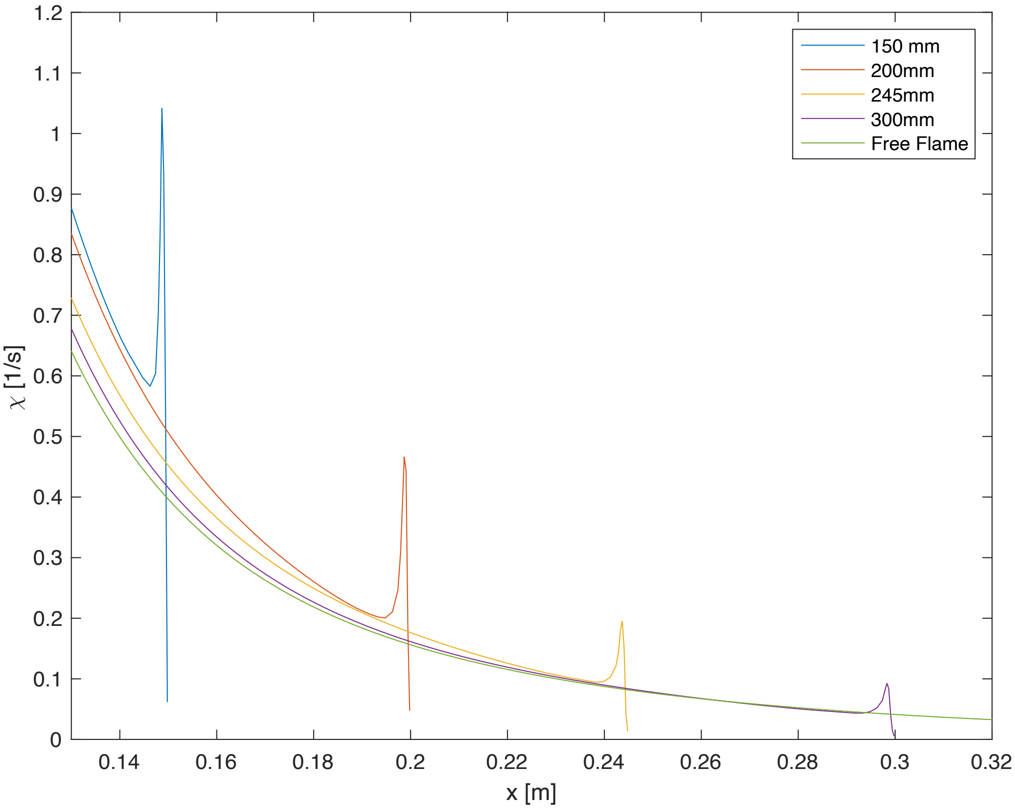

Figure 3.12 Scalar dissipation rate along the centerline for all adiabatic pot surface cases, and free flame case.

Figure 3.12 shows that the scalar dissipation rate is maximum for the 150-mm case and decreases as the surface moves further away from the jet. Note the appearance of a spike in scalar dissipation rate just upstream of the location of the surface. This is because the turbulent energy dissipation rate, ε, is enhanced near the surface. The scalar dissipation rate for a turbulent flamelet is defined as,

$$\chi_t = C_\chi \frac{\varepsilon}{k} \overline{f'^2} \tag{3.8}$$

where C_χ is the constant which is normally 2.0, ε is the turbulent kinetic energy dissipation rate, k is the turbulent kinetic energy, and $\overline{f'^2}$ is the variance of mixture fraction [49].

Since the spikes are where differences arise between cases, it is logical to evaluate the relationship between C_2H_2 and scalar dissipation rate (Figure 3.11) based on the range of the spikes (from the lowest value just before the spike to the peak of the spike). The results are shown in Figure 3.13 by selecting the 150-mm, 245-mm, and 300-mm cases as examples.

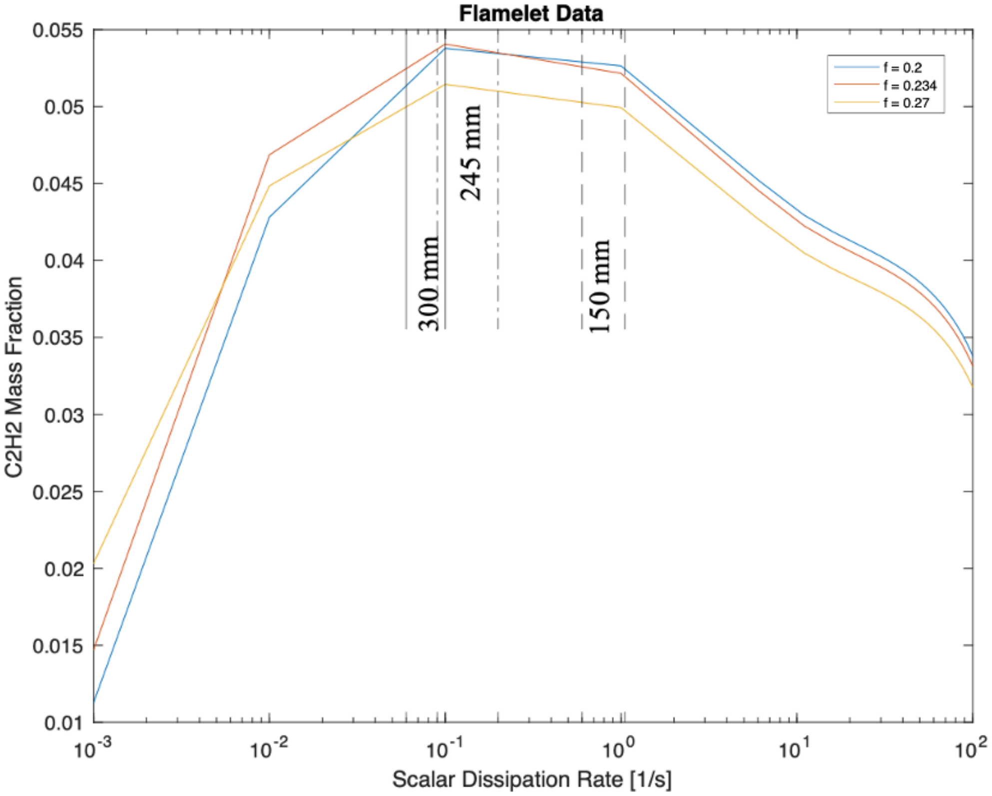

Figure 3.13 Variation of C_2H_2 mass fraction along scalar dissipation rate for f = 0.2, 0.234, and 0.27 with the specified range of scalar dissipation spikes for 150-mm (--), 245-mm (-.), and 300-mm (-) cases.

Figure 3.13 suggests that the value of scalar dissipation rate decreases as the distance between the fuel nozzle and the surface is increased resulting in increasing of C_2H_2 from the 150-mm case to the 245-mm case before decreasing as the surface moves further. Moreover, the 245-mm and 300-mm cases have their centerline scalar dissipation rate spike located where C_2H_2 is maximized. It is worth noting that this behavior resembles that of the C_2H_2 concentration is presented in Table 3.3 where the concentration is plotted against the scalar dissipation rate.

Since the measured soot emission factor and integrated soot flux are based on the processes occurring across the cross-section and not just on the centerline (e.g., Figure 3.12), one approach is to evaluate the average scalar dissipation across the cross-section for each of the cases as a function of axial distance. This essentially takes the idea of Figure 3.12, and extends it across the entire cross-section. The mass-weighted average value of scalar dissipation rate is selected as a representative value which can be expressed,

$$\bar{\chi} = \frac{\int \chi\rho|\vec{v}\cdot d\vec{A}|}{\int \rho|\vec{v}\cdot d\vec{A}|} \qquad (3.9)$$

where ρ is the fluid density, and $\vec{v}$ is the velocity vector that passes through surface $d\vec{A}$. Figure 3.13 shows the mass-weighted average scalar dissipation for all cases.

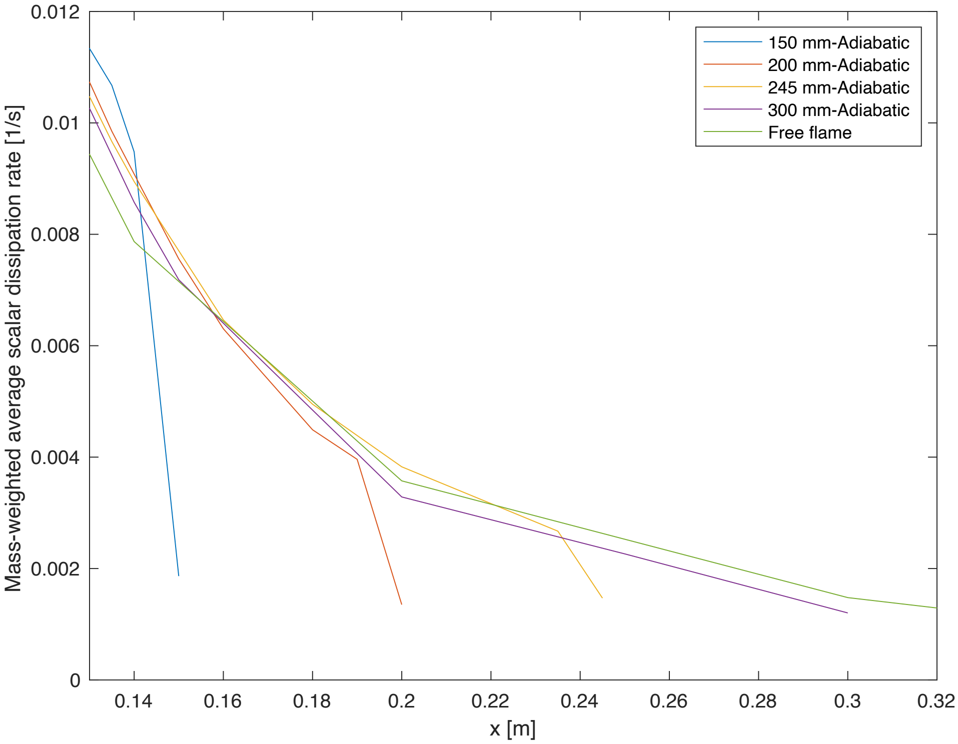

Figure 3.14 Mass-weighted average scalar dissipation rate for all adiabatic pot surface cases and free flame case.

As expected, the mass-weighted average scalar dissipation rate is highest for the case of nozzle-to-surface distance of 150 mm and decreases as the surface moves away from the fuel nozzle. It is worth noting that the mass-weight-average scalar dissipation rate for all cases with a surface also experiences a drastic drop at the surface location. This behavior is observed from the centerline scalar dissipation rate as well.

At this point, it can be concluded that the surface location influences the soot production behavior as placing the surface at different locations results in different scalar dissipation rates. The difference in scalar dissipation rate yields a distinct C_2H_2 concentration field which is the precursor species for surface growth, a dominating process. Moving the surface away from the fuel nozzle lowers the scalar dissipation rate and makes C_2H_2 concentration first increase and then decrease. Moreover, the effect of heat transfer has been determined as the cold surface quenches the surface growth process resulting in reducing soot emission. The study in this chapter is not only beneficial in gaining insight into the soot manufacturing process but can also be used as a guideline for designing the turbulent diffusion flame devices, for example, installing a surface at the location where the soot emission is minimized.

Chapter 4

Modeling of Soot Formation in Flames Impinging on a Cold Surface Part II

4.1 Overview

The scope of this chapter covers two topics: (1) the continued investigation on the integrated soot flux behavior, focusing on the enhancement of oxidation near the impingement surface, and (2) an examination of the behavior of the particle size distributions. The same fixed-pivot sectional model used previously is employed in this chapter.

4.2 Introduction

The integrated soot flux reported in Chapter 3 showed a sharp drop near the impingement surface. Figure 4.1 presents this plot for the convenience of the reader.

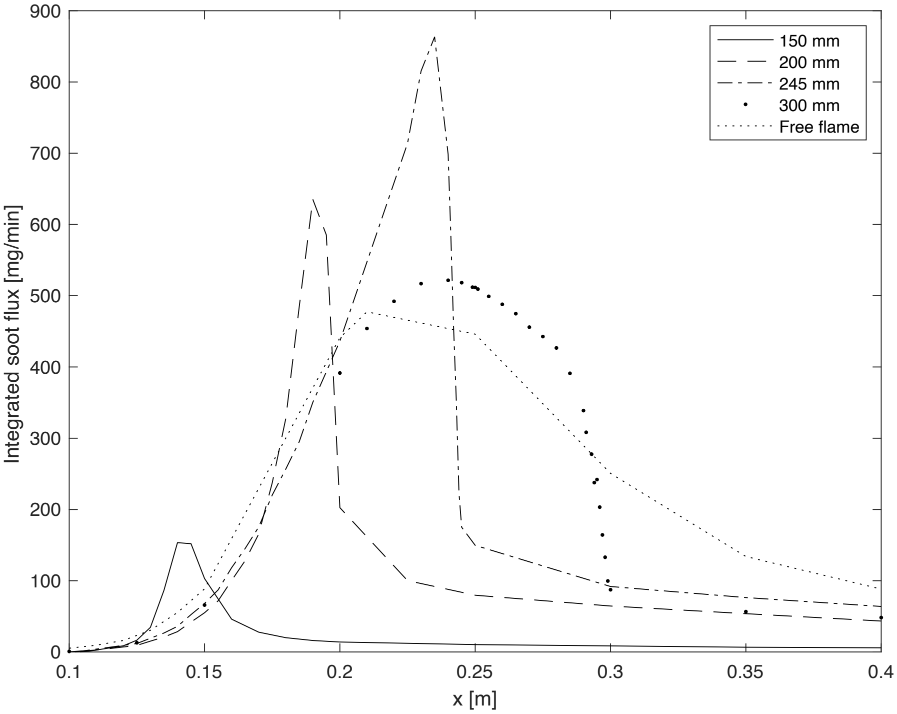

Figure 4.1 Calculated integrated soot flux (mg/min) of adiabatic pot surface cases and free flame case.

One interpretation of the sharp decrease in soot flux shown in Figure 4.1 is that the rapid divergence of the flow just upstream of the surface creates a thin flame which allows more O_2 to diffuse into the flame. The O_2 oxidation process is thus amplified causing the in-flame integrated soot flux to drastically decline. This chapter aims to quantitatively test this hypothesis.

In the previous chapter, the influence of inserting a surface into a turbulent diffusion flame on the behavior of soot, and especially the emission of soot is investigated. Beyond just the emission values, the presence of the surface may influence the soot particle size distribution function, for example through changing the relative importance of the nucleation versus surface growth versus coagulation pathways. This is important as the health effects associated with particulate matter inhalation are strongly influenced by the size of the particles. The experimental flame results presented in Chapter 3 were complemented by the collection of particle size distribution data for the emitted particles. Just as the change in emissions due to surface impingement had not previously been studied, likewise, the modification of the particle size distribution has also not been reported in the literature. The development of a generalized understanding of the controlling processes will ultimately help understand the physics governing size distributions in the cookstove application. Thus, the goal is a mechanistic understanding of the controlling factors for particle size distribution during the impingement of a flame on a surface.

In the present work, the set of flames employed in Chapter 3 are examined focusing on soot characteristics, both in-flame and at the emission point. The source terms and the concentration field of the related species are investigated. The influence of the surface location, as well as the presence or absence of heat transfer, is studied. Furthermore, the mechanisms responsible for the variation of the PSDF are identified.

4.3 Study Approach

The present approach focuses on the investigation of the source terms. Since the surface-integrated soot flux is of interest, the related surface-integrated, the related source terms are examined using the fixed pivot sectional model which is described in Section 3.3. As the process responsible for the behavior is identified, the related species concentration field is investigated and analyzed to obtain the explanation that underlies the interested integrated soot flux behavior.

Another objective of this chapter is to study the influence of inserting a cold surface into flames on the soot particle size distribution. In the present work, the flames from the previous chapter are computationally studied. The same fixed-pivot sectional method which is employed previously is used as a means to provide insight into the development of the particle size distribution. First, the calculated result is verified with the in-house experimental data measured with the scanning mobility particle sizer (SMPS) from the work of Pundle [5]. To expand the scope of work from [5], the comparisons between the adiabatic- and non-adiabatic-surface cases are conducted. This allows the influence of the heat transfer to be identified. Then, significant source terms of soot formation/destruction processes are examined to address the mechanism underlying the phenomenon.

4.4 Results and Discussion

The results of the two goals (soot flux behavior and particle size distributions) are discussed in the next two subsections.

4.4.1 Investigation on the Integrated Soot Flux

Figure 4.1 shows that the peaks of the integrated soot flux peak near the surface location, followed by a rapid decay. For the case of 150-mm to 245-mm, the peaks are located close to the surface, while the peak of the 300-mm case is situated slightly upstream of the surface. The peaks are the results of the spikes in scalar dissipation rate observed in Figure 3.21 which creates high C_2H_2 concentrations in the flamelet data. The peak of the 300-mm case is, however, lower than that of the 245-mm case. This is mainly because the 300-mm case has the surface placed beyond the location where the C_2H_2 has peaked. Thus, the influence of the surface in promoting C_2H_2-driven surface growth is diminished. In all cases the presence of the surface produces a substantial drop in soot flux which does not appear in the free-flame case. The hypothesis presented in Section 4.2 states that inserting the surface into the flame forces the flame to spread around it which allows more O_2 penetration resulting in enhanced O_2 oxidation. One approach to investigate this hypothesis is analyzing the related source term. Since the behavior of the integrated soot flux across the sectional area is of interest, the magnitude of the surface integration of the O_2 oxidation source term for the 245-mm case is shown in Figure 4.2.

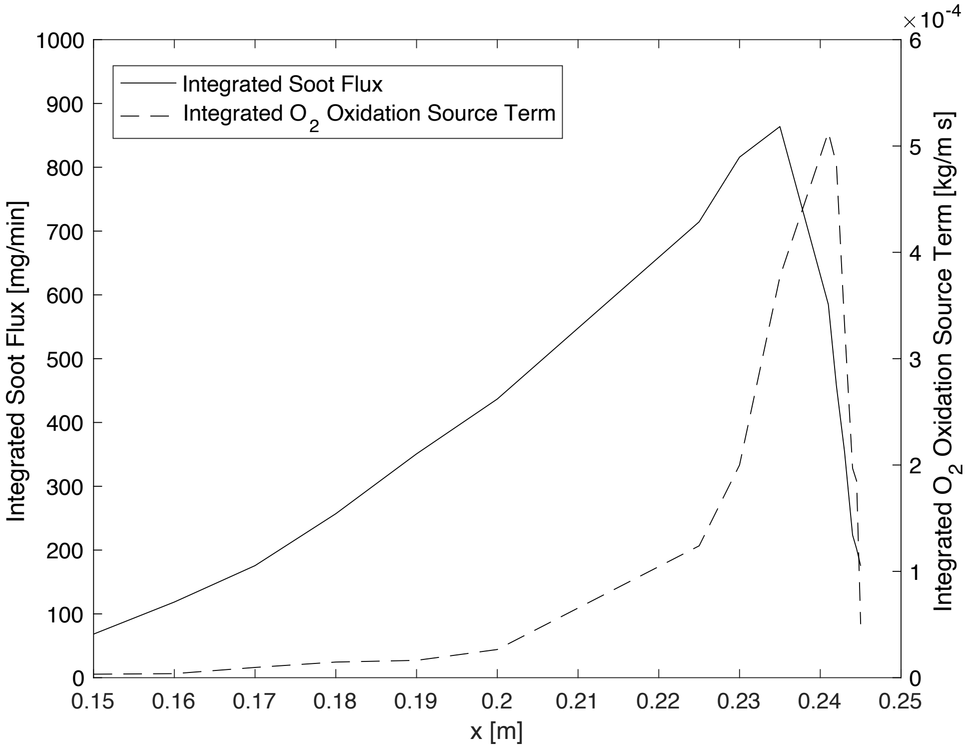

Figure 4.2 Calculated surface-integrated soot flux (mg/min) and the surface-integrated O_2 oxidation source term (magnitude) of the 245-mm-adiabatic-surface case.

Figure 4.2 shows that the magnitude of the surface integration of O_2 oxidation source term increases in the region where the in-flame integrated soot flux declines. This leads to the hypothesis which the substantial drop of the in-flame integrated soot flux is the result of the enhancement in the O_2 oxidation process as the flame spreads around the surface forming a thinner O_2 concentration boundary layer allowing more of such a species to diffuse in. To explore this, the concentration of O_2 is examined. The previous approach of using the integrated flux is not useful here since O_2 is present in the environment surrounding the flame. Instead, we examine the O_2 concentration on the streamline passing though the point of maximum soot concentration. This is taken to be representative of O2 behavior in the region of maximum interaction with the soot. Figure 4.3 presents the variation of O_2 mass fraction along with the axial location for the average streamline passing the highest soot concentration area of the 245-mm-adiabatic-surface and free-flame cases.

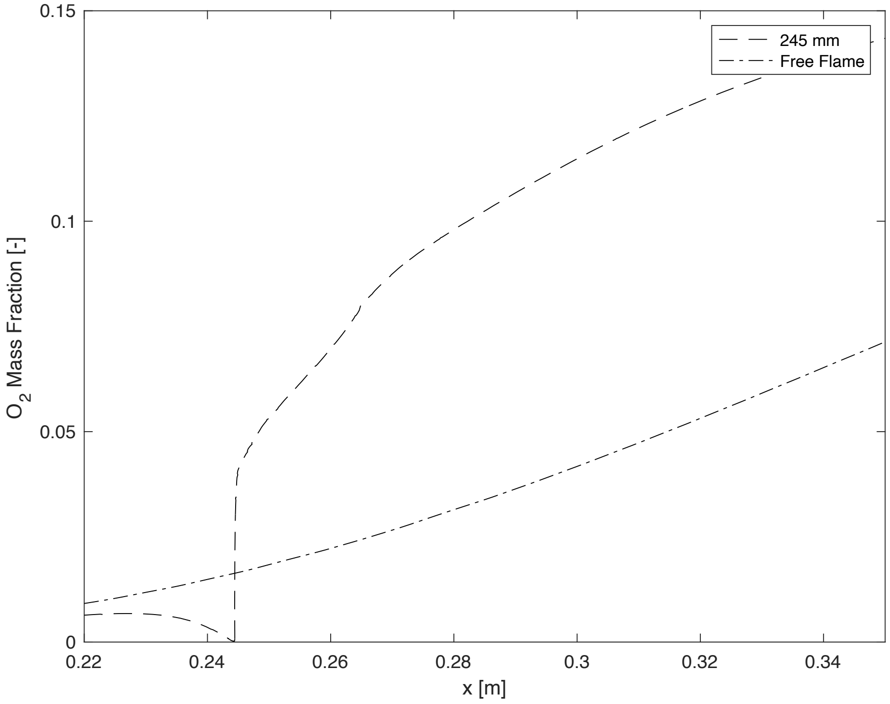

Figure 4.3 The variation of O_2 mass fraction of the average streamline passing through the maximum soot region along the axial location for the 245-mm-adiabatic-surface case and the free-flame case.

Figure 4.3 shows that the O_2 concentration for the 245-mm case increases dramatically near the surface in a way not observed in the free-flame case. The concentration of O_2 is also observed to decrease as the flow approaches the surface for the 245-mm case. This is because the flow velocity decreases as it approaches the stagnation region which inhibits the mixing in this area. Another approach to evaluate the present hypothesis is to analyze the O_2 concentration contour plot which is shown in Figure 4.4. The figure is plotted in the range which emphasizes the O_2 concentration boundary layer.

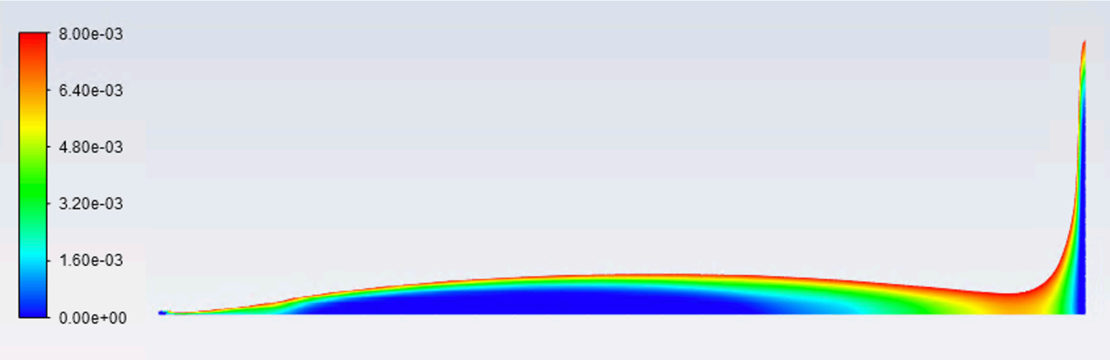

Figure 4.4 The contour plot of O_2 mass fraction of the 245-mm case

Figure 4.4 shows that the concentration boundary layer is significantly thinner at the surface as the flame is spread around the surface allowing more O_2 to diffuse into the flame. Furthermore, the impingement of the jet flame on the surface promotes local entrainment which also introduces more O_2 into the flame as reported by Bruneaux and coworkers [50]. In summary, the post-peak substantial drop in the integrated soot flux is due to an enhancement in O_2 oxidation which is induced by the promotion in both O_2 molecular diffusion and local air entrainment adjacent to the surface location.

4.4.2 Influence of the Cold Surface on the Soot Particle Size Distribution

As mentioned in Section 4.1, aside from studying the effect on soot emission, investigating the influence of a cold surface on the soot particle size is another objective of the present work. Soot particles are widely reported to have an agglomerate structure consisting of individual primary particles collected into chain-like agglomerates. Generally, electrical mobility analyzers [33] are used as the principal means of measuring soot particle size distributions. Since the data of particle size distribution reported in Pundle et al. [5] were measured by the Scanning Mobility Particle Sizer (SMPS), the working principle of such a device is worth explaining in brief to provide a background to the readers. Figure 4.5 presents a schematic diagram of TSI's SMPS model 3910 which was used in [5].

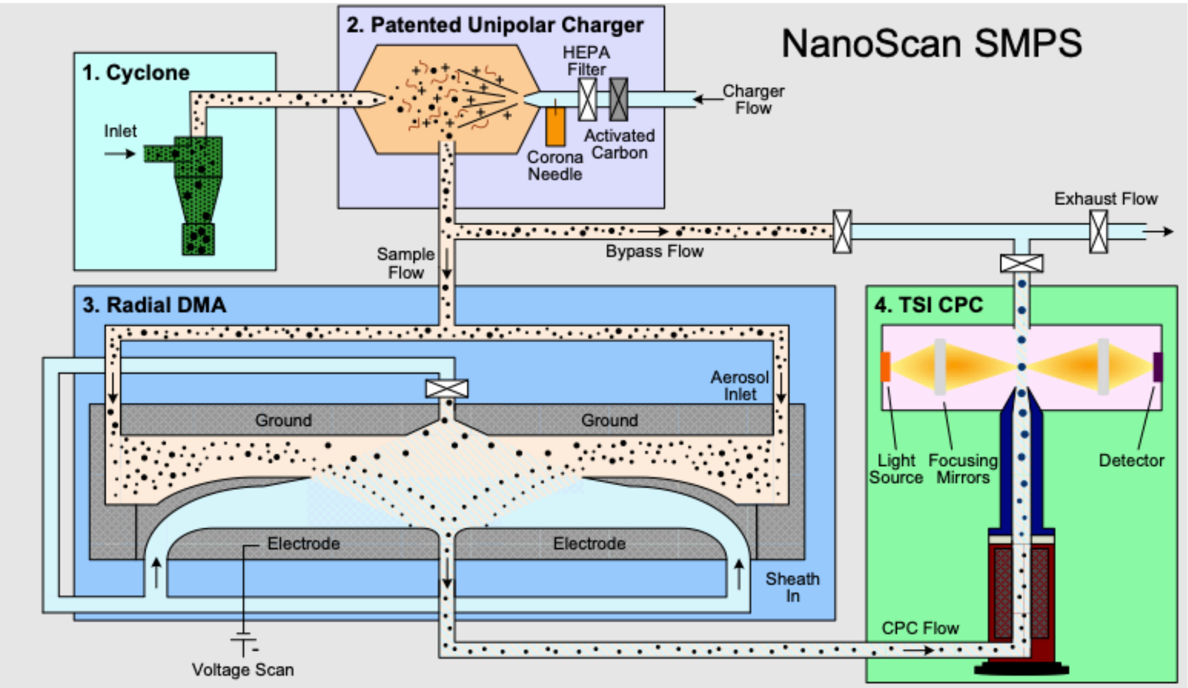

Figure 4.5 The Schematic Diagram of Nanoscan SMPS [9].

This measurement technique is based on (1) the electrostatic charging of particles, and (2) once charged, the motion of the particles in an electrostatic field correlates with particle size. Two additional factors affect operation. First, the charging efficiency depends on particle size, Second, the non-spherical nature of the soot affects the hydrodynamic mobility. Once charged, the particles pass through a Differential Mobility Analyzer (DMA) which differentiates particles based on their electrical mobility which depends on their size. Particles with a monodisperse size distribution are allowed to exit the analyzer. These particles then pass through the particle counter and the concentration of each size distribution is reported. More detail on the SMPS can be found elsewhere [9]. The particle diameter measured by the SMPS is called mobility diameter, the diameter of a spherical particle whose mobility is identical to the agglomerate where the mobility is defined as the ratio between the particle velocity and the force moving the particle [33]. In our work we adopt the spherical assumption which is widely used and reported in several studies [51], [52]. Therefore, the conversion between the simulated spherical result and the measurement data is essentially required to allow the comparison to be made.

Several approaches have been made to convert between the mobility diameter and the simulated spherical diameter. Park and coworkers studied the relationship between soot agglomerate mobility size and mass and the conversion was proposed which can be expressed,

$$M = k_m (\frac{D_{mobility}}{d_p})^{D_{fm}} \tag{4.1}$$

where M is the mass of agglomerates, k_m is the prefactor, $D_{mobility}$ is the mobility diameter, d_p is the primary particle diameter, and D_{fm} is the mobility-based fractal dimension. In such a study, a curve-fit process was conducted to obtain the value of all required parameters in Eqn. 4.1 [53]. As the soot agglomerate mobility size can be converted to mass, the comparison between the measurement data from [5] and the calculated results in this study is made possible. Since the density of the soot particle is assumed to be constant, the spherical diameter can be calculated from the agglomerate mass. As the experiment conducted by Pundle et al. involves heat transfer between the flame and the surface, Figure 4.6 presents the predicted particle size distribution compared to experimental data from [5] for a cold surface located at 200 mm, 245 mm, and 300 mm above the nozzle.

a)

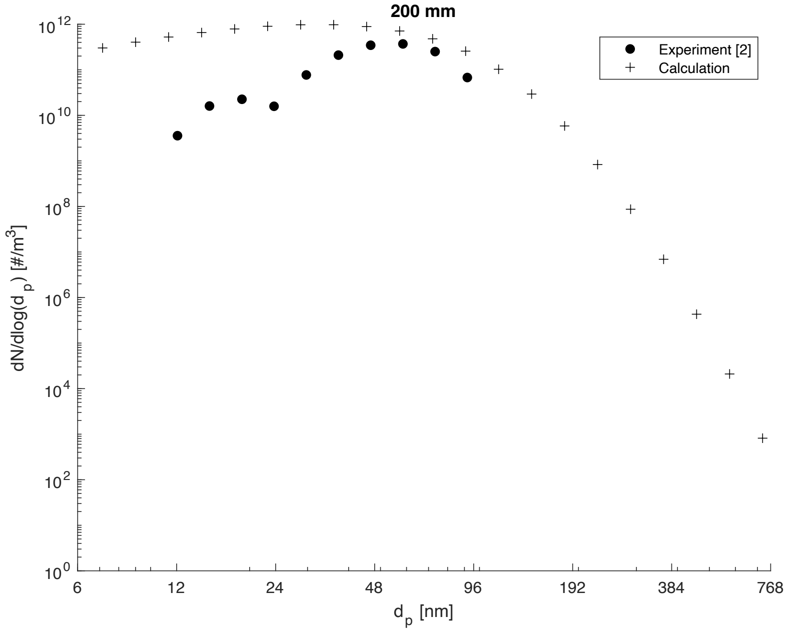
200 mm
Experiment [2]
Calculation
dN/dlog(d_p) [#/m^3]
10^12
10^10
10^8
10^6
10^4
10^2
10^0
6
12
24
48
96
192
384
768
d_p [nm]

b)

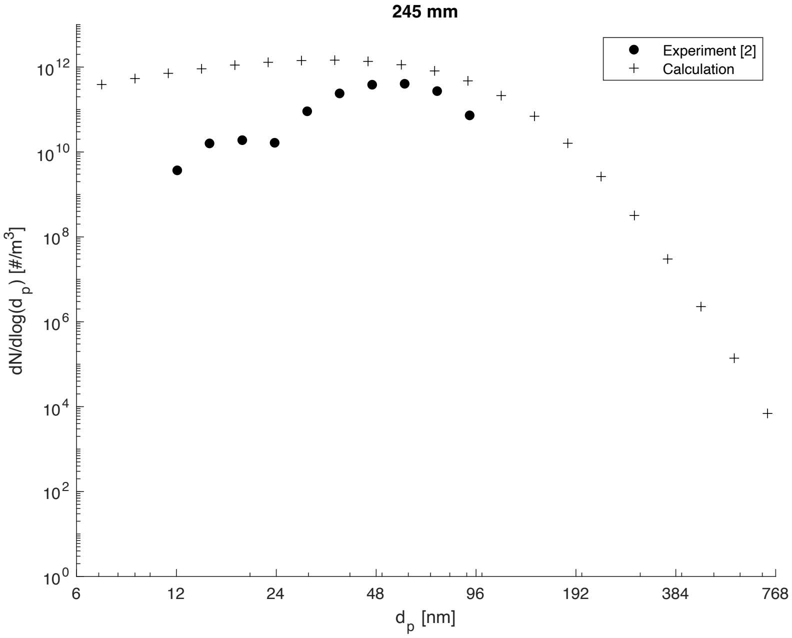
245 mm
Experiment [2]
Calculation
dN/dlog(d_p) [#/m^3]
10^12
10^10
10^8
10^6
10^4
10^2
10^0
6
12
24
48
96
192
384
768
d_p [nm]

c)

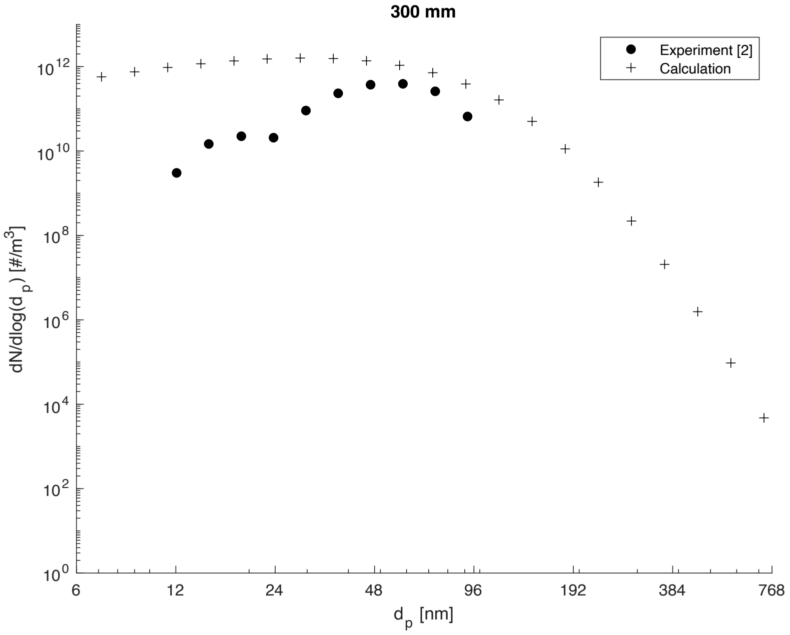

Figure 4.6 Soot particle size distributions from modeling and experimental data [5] for the case where the surface is placed at a) 200 mm, b) 245 mm, and c) 300 mm above the nozzle.

Figure 4.6 shows that the modeling agrees with the trend of the experimental data. The diameter corresponding to the peak of the size distribution and the experimental data are also in good agreement. Hence, the modeling results in this study are validated and used to study the behavior of soot particles in a diffusion flame impinging on a cold surface.

As the present study involves heat transfer between a cold surface and the flame, we are interested in decoupling the effects of fluid dynamics from thermal quench of the gases. As discussed above, we have approached the problem by adopting an adiabatic surface in the model. Figure 4.7 presents the predicted particle size distribution of both adiabatic-surface and nonadiabatic-surface cases.

a)

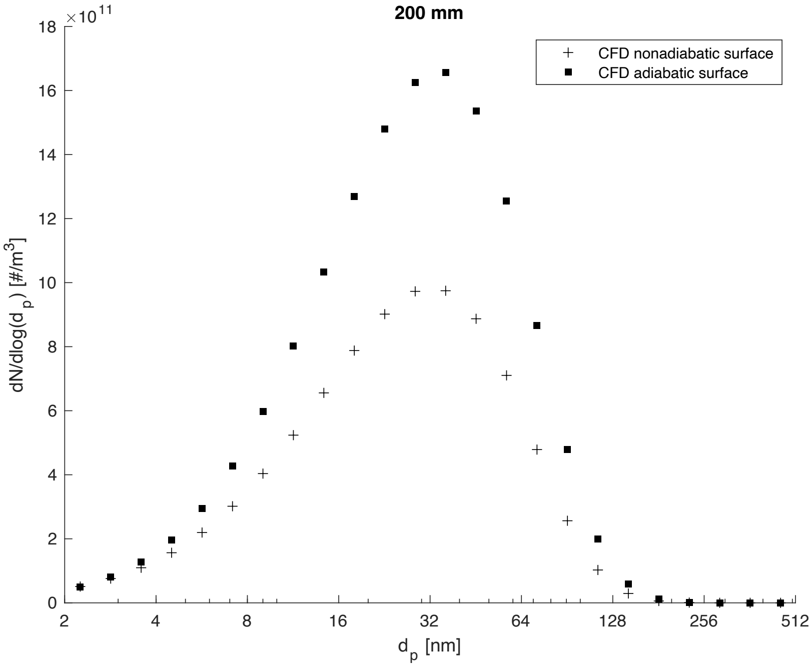
200 mm
×10^11
18
16
14
12
10
8
6
4
2
0
dN/dlog(d_p) [#/m^3]
+ CFD nonadiabatic surface
■ CFD adiabatic surface
2
4
8
16
32
64
128
256
512
d_p [nm]

b)

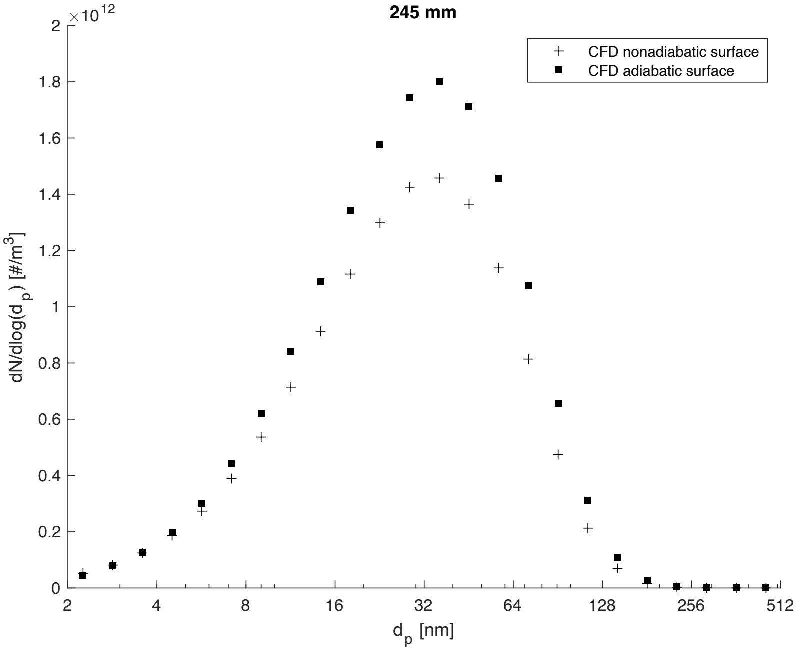
245 mm
×10^12
2
1.8
1.6
1.4
1.2
1
0.8
0.6
0.4
0.2
0
dN/dlog(d_p) [#/m^3]
+ CFD nonadiabatic surface
■ CFD adiabatic surface
2
4
8
16
32
64
128
256
512
d_p [nm]

c)

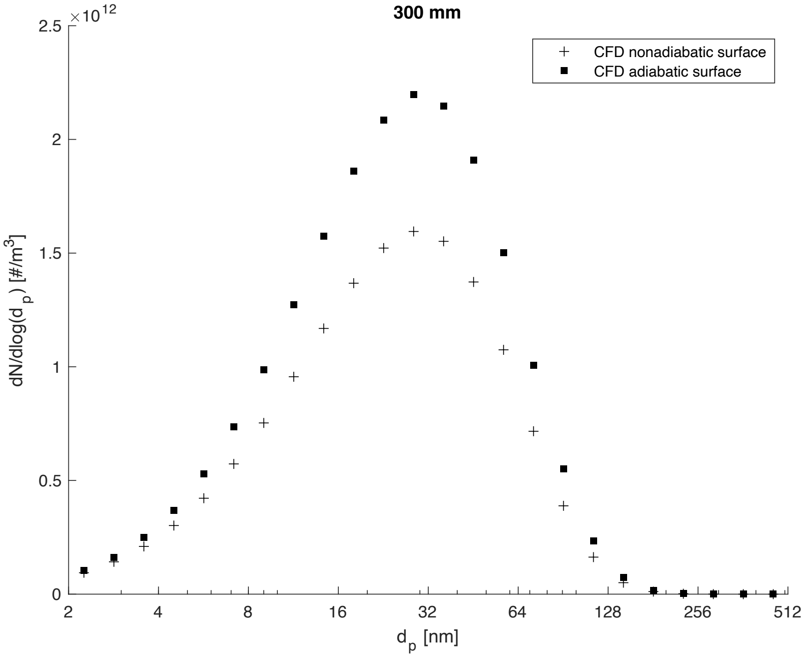

Figure 4.7 Predicted soot particle size distribution for adiabatic and nonadiabatic surface cases where the surface is placed at a) 200 mm, b) 245 mm, and c) 300 mm above the nozzle.

Figure 4.7 shows that for all cases indicate where the heat transfer is eliminated, the mass of soot particles is increased, but no significant difference in the shape of the distribution function is noted. The increase in soot mass is because of the enhanced surface growth process described in Chapter 3.

We also investigated how the surface location influences the soot particle size distribution. Figure 4.8 shows the particle size distribution function for the 200-mm, 245-mm, and 300-mm cases, adiabatic cases are considered to eliminate the effect of heat transfer.

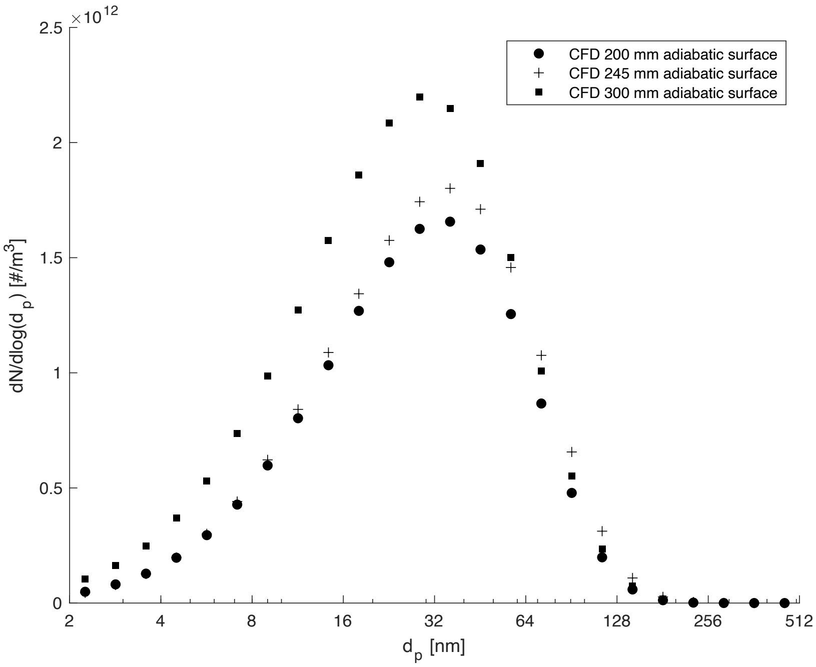

Figure 4.8 Predicted soot particle size distribution for the 200-mm, 245-mm, and 300-mm adiabatic surface cases.

Figure 4.8 illustrates that the 200-mm case has the smallest amount of soot mass among all cases as it experiences the least surface growth process which is mentioned in Chapter 3. An interesting observation arises between the 245-mm and 300-mm cases as the 300-mm case has more small-sized particles than the 245-mm case, nevertheless, has fewer large-sized particles. Therefore, the comparison between both cases needs to be further investigated. According to Chapter 3, the maximum soot mass is reported when the surface is placed at 245 mm above the fuel nozzle. Therefore, this suggests that larger-sized particles make the most contribution to the soot mass. Since the 300-mm case has more small-sized particles, it is rational to infer that more small-sized particles of the 245-mm case are converted to large-sized particles compared to the 300-mm case. The plot suggests that the 300-mm case has more total number of particles than the 245-mm case. Coagulation is the process of interest as it is the only process that enlarges the particle size while reduces the number of the total particles, it is worth investigating how the surface location influences the soot coagulation process.

To identify the effect of surface location on coagulation, the pathline of the particle is considered. In the present study, the pathline which passes through the region of maximum soot concentration is selected as a representative of the soot majority. Since the coagulation rate is generally modeled as a function of temperature and particle concentration [33], both variables are tracked along the mentioned pathline. Variations of temperature along the mentioned pathline are plotted against particle residence time in Figure 4.9.

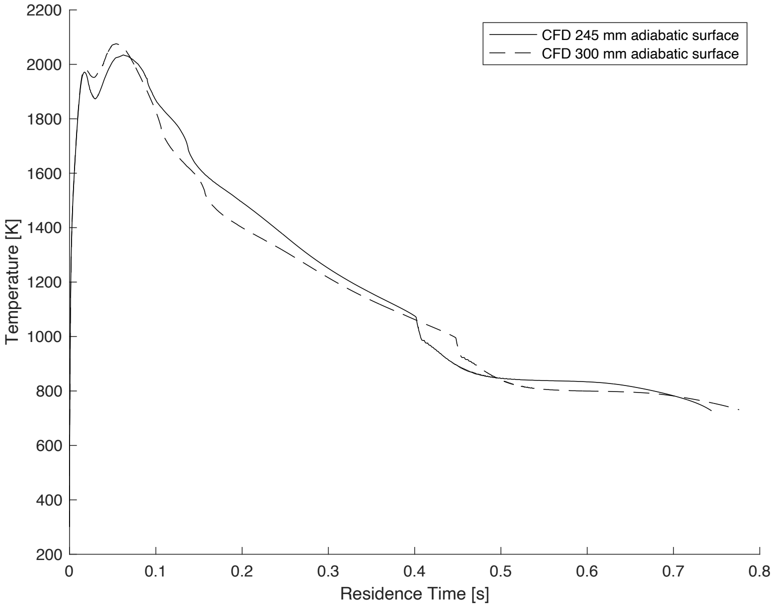

Figure 4.9 Plots of temperature along the particle pathline passing through the maximum soot concentration region for the 245-mm and 300-mm cases.

According to Figure 4.9, there is no significant difference in temperature among cases, therefore, soot concentration is to be considered. Figure 4.10 shows soot concentration for all cases along the same pathline.

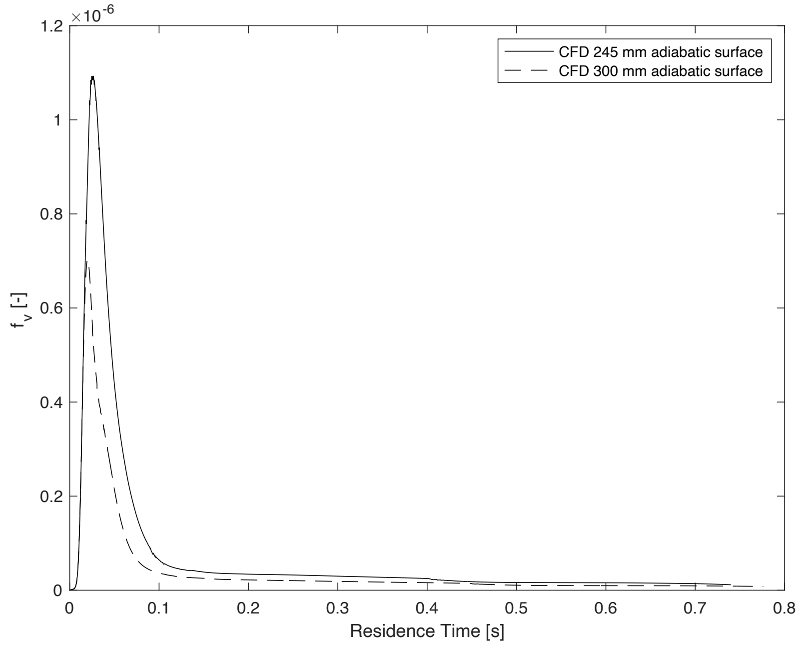

Figure 4.10 Plots of soot volume fraction along the particle pathline passing through the maximum soot concentration region for the 245-mm and 300-mm cases.

Figure 4.10 clearly shows that the 245-mm case presents significantly more soot concentration than the 300-mm case resulting in more collision between particles via the coagulation process, thus reducing the number of particles. This is mainly because the particles are more dispersed for the 300-mm case than the 245-mm case as there is more space between the location where particles are nucleated to the surface.

To conclude this chapter, the observed behavior of the integrated soot flux is investigated. The turbulent scalar dissipation rate spike due to the surface is found to be responsible for the location of the peak integrated soot flux. On the other hand, the dramatic increase in O_2 concentration accompanying the spread of the flame around the surface significantly promotes O_2 diffusion and the enhance entrainment promotes the soot oxidation process.

Besides the integrated soot flux, this chapter studies the influence of inserting a cold surface into turbulent diffusion flame. The heat loss from the flame to the surface reduces the amount of soot emitted, however, it does not affect the size distribution. By comparing the size distribution function between different cases, interesting behavior is observed. The 245-mm case has more soot mass but less total particle number than the 300-mm case. The coagulation process is responsible for the mentioned behavior as the 245-mm case involves more soot concentration resulting in more collision between particles.

Chapter 5

Summary and Conclusions

5.1 Overview

The present work studies the mechanisms of the soot formation process in a turbulent non-premixed ethylene-air flame impinging on a cold surface. The practical motivation for the work is the cookstove problem, particularly the observed enhancement of soot emissions when the flame impinges on the bottom of the cooking pot. The study involves fluid mechanics, heat transfer, combustion, and soot formation. Since this study is based on computational simulation, an accurate and robust model for soot formation is essentially required. Therefore, the present work starts with developing a more accurate model for soot formation in flames, specifically an improvement in the approach for modeling the thermal deactivation of soot towards O_2 oxidation. The rest of this dissertation uses this newly developed model to computationally study the influence of the flames impinging on a cold surface on soot behavior. The study is based on the configuration in the experiment in the work of Pundle et al. [5] which was motivated by the biomass-burning cookstove problem.

5.2 Soot Thermodeactivation Model Development

Soot dynamics in flames is generally considered to consist of 5 main subprocesses: nucleation, surface growth, coagulation, and oxidation by O_2 and OH. While most of the models for these processes are widely validated, the model of the soot O_2 oxidation process, is in need of improvement. Computational modeling has generally indicated that the soot oxidation rate by O_2 is overpredicted which generally causes an underprediction of soot concentrations in the latter stages of non-premixed flames. One challenge is that most O_2 oxidation models are not fundamentally developed but instead are empirical-based models. The soot oxidation process by O_2 is widely known to be complex.

The soot surface becomes less reactive towards reaction (both surface growth and oxidation) as the particle experiences thermal aging. Several attempts have been made to address this reactivity-reducing observation. One of the approaches to model soot surface aging phenomenon was developed by Appel, Bockhorn, and Frenklach (ABF), which focused on the surface growth process. The model is defined in a way that the reactivity is a function of local temperature and particle size. The model assumes that the residence time can be represented by the particle size. The model has been succeeding in predicting the O_2 oxidation effect in premixed flames. However, as the model has been less successful in calculating the oxidation process in non-premixed flames. One reason for this is that in the non-premixed flame, O_2 oxidation is one of the major processes and it reduces the size of the particle, hence, the assumption made in the ABF model is not suitable.

Another model which was recently developed is called the *Thermal Age* model. This model is based on the widely accepted idea that the surface aging process is a function of residence time and temperature. The authors defined a thermal age parameter as a linear function of the temperature and residence time experienced by the particle. The aging process would not, however, generally be expected to be a linear function of temperature. Thus, assuming a linear form in the model is not physically intuitive. Moreover, this model generates an artifact in that a new-born soot particle is calculated to be nonreactive which is counterintuitive since newly nucleated particle must be fully reactive. Therefore, this model still needs improvement.

To achieve an improved model, the coal char surface deactivation model is adapted as a framework to model the soot-O_2 oxidation process due to the similarity between carbonaceous char and carbonaceous soot. This *Thermodeactivation* model is defined in a way that the reactivity has a realistic Arrhenius temperature dependance. Although the functional form is adopted from the coal char surface deactivation process, parameters in the model are expected to be slightly different. One approach to obtain the parameters is to use the existing coal char functional form and adjust the parameters via comparisons against well-defined data sets.

The values of parameters for the newly developed model are obtained by modeling the experimental flame of Pundle et al. During this process, sensitivity analysis is conducted, and it is found that the reactivity is most sensitive to the deactivation energy, E_d. Only a small adjustment in E_d from the literature coal char values yields a good agreement between the simulation results and the experimental data. The newly developed model is then tested against ethylene-air turbulent non-premixed flames in the literature which gives a good agreement. Hence, the *Soot Thermodeactivation* model developed in Chapter 2 is validated.

5.3 Modeling of Soot Formation in Flames Impinging on a Cold surface Part I

Pundle et al. experimentally studied the soot behavior of turbulent ethylene/air non-premixed flames impinging on a water-filled pot. The study reported that the amount of soot emission varies with the distance between the cold surface and the fuel nozzle. The author speculated that as the surface moves away from the nozzle, more surface growth process is allowed due to the higher flame temperature. However, at a certain distance, moving the cold surface further away reduces the emission. The study suggested that this is because the oxidation process is not inhibited as the cold surface is placed outside the oxidation zone.

Chapter 3 employs a CFD model coupled with the new O_2 oxidation model described in Chapter 2 to predict the *soot emissions factor*. The simulation domain is designed to match the experiment by modeling an axisymmetric turbulent ethylene/air non-premixed flame impinging on the cold surface. The distance between the surface and the fuel nozzle is varied between 150 mm, 200 mm, 245 mm, and 300 mm. This study also extends the scope of the investigation to cover the free-flame case to allow for comparisons.

The impingement of the flame on the surface involves both thermal quench via heat extraction and a severe distortion of the flow field. To separate these effects, runs were made in which the surface was set to be adiabatic. If thermal quenching of soot oxidation is responsible for the enhanced emissions, these runs would be expected to produce less soot emissions. The adiabatic runs, however, produced higher soot emissions, suggesting that the higher experimental emissions observed with surface impingement were not due to a quenching of the oxidation.

The alternative is that the enhancement in soot emissions is due to the modification of the fluid flow caused by the surface impingement. One approach to investigate the effect is to examine the magnitude of the various source terms in the soot balance. This was done by evaluating the volume integration of each source term throughout the domain. The findings are summarized as follows.

- The imposition of the surface leads to a substantial increase in the local mixing rate upstream of the surface, in the region where soot formation is active. This is reflected in a substantially increased scalar dissipation rate in this region relative to the unperturbed free flame case. This is principally due to an increase in the turbulent kinetic energy term in this region.
- The chemistry responds to the increased scalar dissipation by generating a higher concentration of acetylene within the laminar flamelet model.
- Acetylene is the species primarily responsible for surface growth in soot particles. Thus, an enhanced acetylene concentration leads to more soot surface growth and a higher soot flux than is present in the free flame case.

The model thus suggests that the more active mixing present upstream of the surface results in more active soot formation chemistry due to a higher concentration of active precursors.

5.4 Modeling of Soot Formation in Flames Impinging on a Cold surface Part II

Chapter 4 has two main objectives which are (1) further investigation into the mechanisms of in-flame soot behavior and (2) studying the effect of flame impingement on the soot particle size distribution (PSDF). To evaluate the in-flame soot behavior, a parameter called the *in-flame integrated soot flux* is introduced. This parameter represents the axial mass flow rate of soot at each sectional plane that is normal to the flame axis with the unit of mg/min. This variable is provided for all the cases presented in Chapter 3. All of the data show the same pattern. The soot concentration (relative to the free flame) rises to a substantial peak just before the surface, and then the soot concentration falls to a very low level as the flow passes around the surface. The soot peaks are the result of the spike in the turbulent scalar dissipation rate which produces more C_2H_2 as discussed in Chapter 3. The post-peak sharp drop is due to a substantial increase in the oxidation of soot by O_2. This is mainly because the surface forces the flame to spread around itself forming a thinner concentration boundary layer with more surface area. The O_2 then more rapidly diffuses into the soot flow which substantially promotes the oxidation process. Furthermore, the impingement of the jet flame on the surface enhances local entrainment which also compliments the soot oxidation process at the surface.

The influence of flame impingement on the surface on the soot particle size distribution was also examined. This complements data obtained by Pundle et al. The comparisons shown in Chapter 4 indicate good agreement between the datasets and the model in terms of the shape of the particle size distributions and the mean particle size. This present study then further investigates the simulation results.

Comparing the adiabatic and non-adiabatic surface cases showed more soot for the adiabatic cases, as noted in previous chapters, but showed no significant difference in the shape of the size distribution. However, an interesting behavior is found that the 300-mm case has more small-sized particles than the 245-mm case, but fewer large-sized particles. Data shown in Chapter 3 indicates that the 245-mm case creates the most soot Therefore, the 245-mm case provides more opportunity for coagulation than the other cases. This converts smaller particles into larger particles while reducing the total number of particles. This results in the observed shift of the particle size distribution.

5.5 Future Work

In the present work, the scope of this study is limited to the ethylene/air flame. Even though the model employed is generic and expected to be able to predict the effect of other gas-phase fuels. It would be beneficial to investigate whether the model can accurately predict the behavior of soot particles with a variety of fuel choices. Being able to apply the model to other fuels can be useful as the effect on soot particles can be predicted from other fuel-based combustion applications.

Finally, this study reports that the surface location, as well as the heat extraction from the flame, can influence the soot behavior. Finding a generic form of relationship between the soot behavior and the affecting variable, for example, the amount of soot as a function of flame variables, and surface dimensions, could be advantageous. This knowledge can be adapted to the process of designing the application in which the soot formation is concerned to control both the amount and the size of the emission.

References

[1] J. Appel, H. Bockhorn, and M. Frenklach, "Kinetic modeling of soot formation with detailed chemistry and physics in premixed hydrocarbon flames," *Combust. Flame*, vol. 121, no. 1–2, pp. 122–136, 2000.

[2] A. Khosousi and S. B. Dworkin, "Detailed modelling of soot oxidation by O2and OH in laminar diffusion flames," *Proc. Combust. Inst.*, vol. 35, no. 2, pp. 1903–1910, 2015, doi: 10.1016/j.proci.2014.05.152.

[3] A. Veshkini, S. B. Dworkin, and M. J. Thomson, "A soot particle surface reactivity model applied to a wide range of laminar ethylene/air flames," *Combust. Flame*, vol. 161, no. 12, pp. 3191–3200, 2014, doi: 10.1016/j.combustflame.2014.05.024.

[4] B. Sullivan, G. Allawatt, A. Emery, P. Means, J. Kramlich, and J. Posner, "Time-Resolved Particulate Emissions Monitoring of Cookstove Biomass Combustion Using a Tapered Element Oscillating Microbalance," *Combust. Sci. Technol.*, vol. 189, no. 6, pp. 923–936, 2017, doi: 10.1080/00102202.2016.1253564.

[5] A. Pundle, "Combustion, heat transfer and soot formation in cookstoves," University of Washington, 2019.

[6] F. Xu, P. Sunderland, and G. Faeth, "Soot formation in laminar premixed ethylene/air flames at atmospheric pressure," *Combust. Flame*, vol. 108, no. 4, pp. 471–493, 1997.

[7] J. H. Kent and D. Honnery, "Soot and Mixture Fraction in Turbulent Diffusion Flames," *Combust. Sci. Technol.*, vol. 54, no. 1–6, pp. 383–398, 1987, doi:

10.1080/00102208708947062.

[8] K. J. Young, C. D. Stewart, K. J. Syed, and J. B. Moss, “Soot formation in confined turbulent flames fuelled by pre-vaporised kerosine and by ethylene,” *Proc. Tenth ISABE Meet. AIAA*, p. 239, 1991.

[9] TSI Incorporated, “Nanoscan SMPS, nanoparticle sizer, theory of operation (Application Note SMPS-005).” [Online]. Available: https://tsi.com/getmedia/b2cdf436-3299-496e-b067-59bc18937e76/NanoScan_SMPS_Theory_of_Operation_US_SMPS-005A-web?ext=.pdf.

[10] O. Senneca and P. Salatino, “Loss of gasification reactivity toward O2 and CO2 upon heat treatment of carbons,” *Proc. Combust. Inst.*, vol. 29, no. 1, pp. 485–493, 2002, doi: 10.1016/s1540-7489(02)80063-3.

[11] W. H. Organization, “Household air pollution and health,” 2018. [Online]. Available: https://www.who.int/news-room/fact-sheets/detail/household-air-pollution-and-health.

[12] K. H. Homann and H. G. G. Wagner, “Some new aspects of the mechanism of carbon formation in premixed flames,” *Symp. Combust.*, vol. 11, no. 1, pp. 371–379, 1967, doi: 10.1016/S0082-0784(67)80161-9.

[13] B. S. Haynes and H. G. Wagner, “Soot formation,” *Prog. Energy Combust. Sci.*, vol. 7, no. 4, pp. 229–273, 1981, doi: 10.1016/0360-1285(81)90001-0.

[14] M. Frenklach, “Reaction mechanism of soot formation in flames,” *Phys. Chem.*

Chem. Phys., vol. 4, no. 11, pp. 2028–2037, 2002, doi: 10.1039/b110045a.

[15] M. Frenklach and H. A. I. Wang, "Detailed Modeling of Soot Particle Nucleation and Growth," *Proc. Combust. Inst.*, vol. 23, no. 1, pp. 1559–1566, 1991.

[16] C. F. Melius, M. E. Colvin, N. M. Marinov, W. J. Pit, and S. M. Senkan, "Reaction mechanisms in aromatic hydrocarbon formation involving the C5H5 cyclopentadienyl moiety," *Symp. Combust.*, vol. 26, no. 1, pp. 685–692, 1996, doi: 10.1016/S0082-0784(96)80276-1.

[17] M. J. Castaldi *et al.*, "Experimental and modeling investigation of aromatic and polycyclic aromatic hydrocarbon formation in a premixed ethylene flame," *Symp. Combust.*, vol. 26, no. 1, pp. 693–702, 1996, doi: 10.1016/S0082-0784(96)80277-3.

[18] M. B. Colket and D. J. Seery, "Reaction mechanisms for toluene pyrolysis," *Symp. Combust.*, vol. 25, no. 1, pp. 883–891, 1994, doi: 10.1016/S0082-0784(06)80723-X.

[19] M. Frenklach, T. Yuan, and M. K. Ramachandra, "Soot Formation in Binary Hydrocarbon Mixtures," *Energy and Fuels*, vol. 2, no. 4, pp. 462–480, 1988, doi: 10.1021/ef00010a013.

[20] M. Fairweather *et al.*, "Predictions of Soot Formation In Turbulent, Non-Premixed Propane Flames," *Symp. Combust.*, pp. 1067–1074, 1992.

[21] A. Khosousi and S. B. Dworkin, "Soot surface reactivity during surface growth and oxidation in laminar diffusion flames," *Combust. Flame*, vol. 162, no. 12, pp. 4523–4532, 2015, doi: 10.1016/j.combustflame.2015.09.005.

[22] J. Nagle and R. Strickland-Constable, "No Title," in *Proceedings of the Fifth*

Conference on Carbon, 1962, p. 154.

[23] K. G. Neoh, J. B. Howard, and A. F. Sarofim, "Soot Oxidation in Flames," *Part. Carbon*, pp. 261–282, 2013, doi: 10.1007/978-1-4757-6137-5_9.

[24] M. D. Smooke, C. S. McEnally, L. D. Pfefferle, R. J. Hall, and M. B. Colket, "Computational and experimental study of soot formation in a coflow, laminar diffusion flame," *Combust. Flame*, vol. 117, no. 1–2, pp. 117–139, 1999, doi: 10.1016/S0010-2180(98)00096-0.

[25] G. Blanquart, P. Pepiot-Desjardins, and H. Pitsch, "Chemical mechanism for high temperature combustion of engine relevant fuels with emphasis on soot precursors," *Combust. Flame*, vol. 156, no. 3, pp. 588–607, 2009, doi: 10.1016/j.combustflame.2008.12.007.

[26] K. Netzell, H. Lehtiniemi, and F. Mauss, "Calculating the soot particle size distribution function in turbulent diffusion flames using a sectional method," *Proc. Combust. Inst.*, vol. 31 I, no. 1, pp. 667–674, 2007, doi: 10.1016/j.proci.2006.08.081.

[27] Z. Wen, S. Yun, M. J. Thomson, and M. F. Lightstone, "Modeling soot formation in turbulent kerosene / air jet diffusion flames," vol. 135, pp. 323–340, 2003, doi: 10.1016/S0010-2180(03)00179-2.

[28] S. H. Park and S. N. Rogak, "A novel fixed-sectional model for the formation and growth of aerosol agglomerates," *J. Aerosol Sci.*, vol. 35, no. 11, pp. 1385–1404, 2004, doi: 10.1016/j.jaerosci.2004.05.010.

[29] M. Frenklach and H. Wang, "Detailed Mechanism and Modeling of Soot Particle

Formation," *Soot Form. Combust.*, pp. 165–192, 1994, doi: 10.1007/978-3-642-85167-4_10.

[30] J. Z. Wen, M. J. Thomson, M. F. Lightstone, S. H. Park, and S. N. Rogak, "An improved moving sectional aerosol model of soot formation in a plug flow reactor," *Combust. Sci. Technol.*, vol. 178, no. 5, pp. 921–951, 2006, doi: 10.1080/00102200500270007.

[31] S. KUMAR and D. RAMKRISHNA, "On the solution of population balance equations by discretization—I. A fixed pivot technique," *Chem. Eng. Sci.*, vol. 51, no. 8, pp. 1311–1332, 1996.

[32] F. Xu, A. M. El-Leathy, C. H. Kim, and G. M. Faeth, "Soot surface oxidation in hydrocarbon/air diffusion flames at atmospheric pressure," *Combust. Flame*, vol. 132, no. 1–2, pp. 43–57, 2003, doi: 10.1016/S0010-2180(02)00459-5.

[33] S. K. Friedlander, *Smoke, Dust, and Haze: Fundamentals of Aerosol Behavior*. New York: Wieley Interscience, 1977.

[34] J. S. Bhatt and R. P. Lindstedt, "Analysis of the impact of agglomeration and surface chemistry models on soot formation and oxidation," *Proc. Combust. Inst.*, vol. 32, no. 1, pp. 713–720, 2009, doi: 10.1016/j.proci.2008.06.201.

[35] A. Kazakov, H. Wang, and M. Frenklach, "Detailed modeling of soot formation in laminar premixed ethylene flames at a pressure of 10 bar," *Combust. Flame*, vol. 100, no. 1–2, pp. 111–120, 1995, doi: 10.1016/0010-2180(94)00086-8.

[36] R. L. Vander Wal and A. J. Tomasek, "Soot oxidation: Dependence upon initial

nanostructure," *Combust. Flame*, vol. 134, no. 1–2, pp. 1–9, 2003, doi: 10.1016/S0010-2180(03)00084-1.

[37] M. Frenklach, Z. Liu, R. I. Singh, G. R. Galimova, V. N. Azyazov, and A. M. Mebel, "Detailed, sterically-resolved modeling of soot oxidation: Role of O atoms, interplay with particle nanostructure, and emergence of inner particle burning," *Combust. Flame*, vol. 188, pp. 284–306, 2018, doi: 10.1016/j.combustflame.2017.10.012.

[38] W. R. Smith and M. H. Polley, "The oxidation of graphitized carbon black," *J. Phys. Chem.*, vol. 60, no. 5, pp. 689–691, 1956, doi: 10.1021/j150539a046.

[39] P. Salatino, O. Senneca, and S. Masi, "Assessment of thermodeactivation during gasification of a bituminous coal char," *Energy and Fuels*, vol. 13, no. 6, pp. 1154–1159, 1999, doi: 10.1021/ef9900334.

[40] O. Senneca, P. Russo, P. Salatino, and S. Masi, "The relevance of thermal annealing to the evolution of coal char gasification reactivity," *Carbon N. Y.*, vol. 35, no. 1, pp. 141–151, 1997, doi: 10.1016/S0008-6223(96)00134-0.

[41] S. B. Dworkin, Q. Zhang, M. J. Thomson, N. A. Slavinskaya, and U. Riedel, "Application of an enhanced PAH growth model to soot formation in a laminar coflow ethylene / air diffusion flame," *Combust. Flame*, vol. 158, no. 9, pp. 1682–1695, 2011, doi: 10.1016/j.combustflame.2011.01.013.

[42] S. H. Park, S. N. Rogak, W. K. Bushe, and J. Z. Wen, "Combustion Theory and Modelling An aerosol model to predict size and structure of soot particles," *Combust. Theory Model.*, pp. 37–41, 2007, doi: 10.1080/13647830500195005.

[43] M. S. Celnik, M. Sander, A. Raj, R. H. West, and M. Kraft, “Modelling soot formation in a premixed flame using an aromatic-site soot model and an improved oxidation rate,” *Proc. Combust. Inst.*, vol. 32, no. 1, pp. 639–646, 2009, doi: 10.1016/j.proci.2008.06.062.

[44] F. R. Menter, M. Kuntz, and R. Langtry, “Ten Years of Industrial Experience with the SST Turbulence Model,” *Turbul. Heat Mass Transf. 4*, vol. 1, pp. 625–632, 2003.

[45] Ansys Inc., “Ansys Fluent Theory Guide,” 2009. [Online]. Available: https://www.afs.enea.it/project/neptunius/docs/fluent/html/th/node156.htm.

[46] F. M. White, *Fluid Mechanics*. McGraw-Hill, 2011.

[47] K. Stephan and A. Laesecke, “The Thermal Conductivity of Fluid Air,” *J. Phys. Chem. Ref. Data*, vol. 14, no. 1, pp. 227–234, 1985, doi: 10.1063/1.555749.

[48] S. Sazhin, “An approximation for the absorption coefficient of soot in a radiating gas,” *Fluent Eur.*, 1994.

[49] W. P. Jones and J. H. Whitelaw, “Calculation methods for reacting turbulent flows: A review,” *Combust. Flame*, vol. 48, no. C, pp. 1–26, 1982, doi: 10.1016/0010-2180(82)90112-2.

[50] G. Bruneaux, M. Causse, and A. Omrane, “Air entrainment in Diesel-like gas jet by simultaneous flow velocity and fuel concentration measurements, comparison of free and wall impinging jet configurations,” *SAE Int. J. Engines*, vol. 5, no. 2, pp. 76–93, 2012, doi: 10.4271/2011-01-1828.

[51] J. Singh, R. I. A. Patterson, M. Kraft, and H. Wang, “Numerical simulation and

sensitivity analysis of detailed soot particle size distribution in laminar premixed ethylene flames," *Combust. Flame*, vol. 145, no. 1–2, pp. 117–127, 2006, doi: 10.1016/j.combustflame.2005.11.003.

[52] R. I. A. Patterson, J. Singh, M. Balthasar, M. Kraft, and W. Wagner, "Extending stochastic soot simulation to higher pressures," *Combust. Flame*, vol. 145, no. 3, pp. 638–642, 2006, doi: 10.1016/j.combustflame.2006.02.005.

[53] K. Park, D. B. Kittelson, and P. H. McMurry, "Structural properties of diesel exhaust particles measured by Transmission Electron Microscopy (TEM): Relationships to particle mass and mobility," *Aerosol Sci. Technol.*, vol. 38, no. 9, pp. 881–889, 2004, doi: 10.1080/027868290505189.